Gas-particle partitioning of m-xylene and naphthalene oxidation products: temperature and NO_x influence

Marwa Shahin[1], Julien Kammer[1], Brice Temime-Roussel[1], and Barbara D'Anna[1]

[1]Aix-Marseille Univ., CNRS, LCE, Marseille, France

Correspondence to: Barbara D'Anna (barbara.danna@univ-amu.fr), Marwa Shahin (marwa.shahin@etu.univ-amu.fr)

Abstract. Volatile organic compounds (VOCs) react with atmospheric oxidants resulting in oxygenated products of lower volatility known as semi and intermediate volatile organic compounds (S/IVOCs) forming secondary organic aerosols (SOA). Those compounds can partition between the gas and particle phases, a critical process influenced by several environmental parameters, yet poorly constrained. This study aims to evaluate the effect of temperature and VOC/NO_x ratio on SOA formation and partitioning of individual SOA products from m-xylene and naphthalene OH-oxidation. Experiments are carried out in an oxidation flow reactor (OFR) and products are identified and quantified using a proton transfer reaction time-of-flight mass spectrometer (PTR-ToF-MS) coupled to a CHemical Analysis of aeRosol ONline (CHARON) inlet. Results show that lower temperatures significantly enhance SOA formation, while lower VOC/NO_x ratios reduce it. Gas-phase m-xylene major products are C_3, C_5 and C_8 whereas particle-product distributions exhibit a progressive increase from C_2 to C_8. In contrast, naphthalene products partition more readily into the condensed phase, with C_8-C_{10} products dominating. Most of the oxidation products from both precursors exhibit a volatility distribution in the SVOC regime, with fewer in the IVOC regime. The decrease in temperature shifts the effective saturation concentration (C_i^*) values towards lower values, though no clear relationship between C_i^* and oxidation state is observed. A comparison between observed and estimated volatilities using a model based on group contribution method (SIMPOL.1) reveals systematic deviations for both light molecules and heavy compounds, suggesting a need for improved predictive models.

1 Introduction

Aromatic hydrocarbons (AHs) are an ubiquitous class of air pollutants and contribute to an important fraction of the total volatile organic compounds (VOCs) in urban environments; the relative contribution may vary and depends on location and season (Calvert et al., 2002; Jiang et al., 2017; Montero-Montoya et al., 2018). Among the different AHs, xylene and naphthalene are important anthropogenic VOCs primarily emitted from petrochemical industries, biomass burning, diesel and gasoline engines, or through solvent evaporation (Fang et al., 2021, 2024; Wu et al., 2020; Xuan et al., 2021). In the atmosphere, AHs react with common oxidants as hydroxyl (OH), nitrate (NO_3) and chloride (Cl) radicals and ozone (O_3) leading to the formation of oxygenated reaction products of lower vapor pressures also known as semi-volatile organic compounds (SVOCs) and intermediate-volatile organic compounds (IVOCs) (Seinfeld and Pandis, 2016). These compounds

may partition to the particle phase forming secondary organic aerosols (SOA) that represent approximately 60% of ambient organic aerosol (Huang et al., 2020, 2014) and have an impact on visibility (Li et al., 2014; Liu et al., 2017), climate (Liu and Matsui, 2020; Shrivastava et al., 2017) and human health (Anderson et al., 2012; Berlinger et al., 2024; Singh and Tripathi, 2021; Thangavel et al., 2022). Indeed, particulate air pollution is closely correlated to the progression of numerous respiratory diseases, in addition to cancer, cardiovascular diseases, and neurological damage (Liu et al., 2022a; Singh and Tripathi, 2021; Song et al., 2017; Thangavel et al., 2022). In the EU, each year, around 238,000 premature deaths are attributable to fine particulate matter ($PM_{2.5}$) exposure (European Environment Agency, 2022). Improving our understanding of particle sources and properties is thus pivotal to improve a more sustainable environment.

Over the last decades, many laboratory and modelling studies investigated SOA generated by AHs reaction products (Chen et al., 2018; Forstner et al., 1997; Klodt et al., 2023; Lannuque et al., 2018; Li et al., 2022; Liu et al., 2023, 2022b; Lu et al., 2024; Song et al., 2007; Srivastava et al., 2022; Tian et al., 2023). The OH radical oxidation of monoaromatic compounds operates through two main common pathways (Atkinson et al., 1991; Bloss et al., 2005; Calvert et al., 2002; Forstner et al., 1997; Pan and Wang, 2014). In the case of m-xylene, the first pathway is the OH radical addition to the aromatic ring, predominantly on the ortho position (Fan and Zhang, 2008) to form a hydroxy-methyl-benzyl radical with a subsequent addition of O_2 to form a bicyclic radical, a major ring opening product channel (Zhao et al., 2005). The second reaction pathway is the H-abstraction from the methyl group to form a methyl benzyl radical, with a subsequent addition of O_2 to form a benzyl peroxy radical (Atkinson et al., 1991; Molina et al., 1999). In the presence of NO_x, the peroxy radical mainly reacts with NO to form an alkoxy radical, and finally an abstraction by O_2 leads to the formation of m-tolualdehyde (Srivastava et al., 2023). In the case of naphthalene, OH radical reaction is initiated exclusively by OH addition, most predominantly at the α-carbon (68 %) adjacent to the fusion of its two aromatic rings (Wang et al., 2007). Then, a hydroxy cyclohexadienyl radical is formed, which further reacts with NO_2 to form nitrogen-containing compounds, or with O_2 to form various products out of which 2-formylcinnamaldehyde is major (Nishino et al., 2009).

The NO_x level has been shown to have significant yet possibly contrasting effects on SOA formation (Chan et al., 2009; Liu et al., 2024; Ng et al., 2007; Qi et al., 2020; Sarrafzadeh et al., 2016; Song et al., 2005; Zhu et al., 2021). Some studies have reported a decrease in SOA yield under high NO_x conditions which can be explained by the termination reactions of NO with the peroxy (RO_2 and HO_2) and OH radicals, limiting the formation of lower volatility compounds (Chan et al., 2009; Ng et al., 2007; Song et al., 2005). Nonetheless, Zhu et al. (2021) reported an increase in SOA mass under elevated levels of NO_x compared to NO_x free experiments. Enhanced SOA formation under high NOx has also been linked to the formation of organic nitrates and the isomerization of alkoxy radicals into low-volatility products, or related to a change in OH concentration due to the presence of NO_x (Ng et al., 2007; Schwantes et al., 2019; Shi et al., 2022; Srivastava et al., 2023). Under low NO_x conditions, RO_2 radicals primarily react with HO_2 to form low-volatility organic hydroperoxides, which contribute to new particle formation and increase SOA mass (Xu et al., 2014; Zhao et al., 2018). These findings illustrate that NO_x is capable of both inhibiting and promoting SOA formation depending on the NO_x regime.

A key process determining the fate of the oxidation products generated from AH oxidation is their ability to partition between gas and particle phases, either throughout nucleation forming new particles or by condensing on pre-existing particles. Partitioning is influenced by many environmental parameters such as temperature, relative humidity, the nature and the diameter of the pre-existing particles on which they condense and the physio-chemical properties of the S/IVOC condensing (Kamens et al., 2011; Kim et al., 2007; Lannuque et al., 2018; Loza et al., 2012; Ng et al., 2007; Qi et al., 2010; Sato et al., 2007; Takekawa et al., 2003; Warren et al., 2009; Xu et al., 2015).

It is well recognized that SOA yields increase at lower temperatures, a trend consistently reported for both terpenes and isoprene (Clark et al., 2016; Deng et al., 2021; Svendby et al., 2008; Virtanen et al., 2010), aromatics (Lannuque et al., 2023; Svendby et al., 2008), alkanes (n-dodecane in Fan et al., 2025; Li et al., 2020) and amines (Price et al., 2016). This behavior is attributed primarily to the decrease of the vapor pressures of the compounds, displacing the equilibrium towards the particle phase. However, the impact of temperature on SOA composition is not fully understood, and seems to depend on other experimental conditions (precursor, seed acidity, etc.). For biogenic precursors, previous studies reported more oligomer formation at lower temperatures (Li et al., 2020; Fan et al., 2025), driven by increased SVOC partitioning and condensed-phase reactions, while others observed the opposite, attributing higher-temperature oligomerization to radical or acid-catalyzed reactions (Clark et al., 2016; Deng et al., 2021; Price et al., 2016). Additionally, Li et al. (2019) highlighted how lower temperatures increase SOA viscosity, suppressing evaporation and favoring retention of low-volatility species. Conversely, Lamkaddam et al., (2017) found a weak temperature sensitivity in SOA formation from n-dodecane, suggesting that extremely low-volatility products and compensating shifts in product types may offset volatility effects. Regarding aromatic compounds, only Lannuque et al. (2023) investigated the effect of temperature on SOA chemical composition at molecular level, showing a general agreement of product distribution between 280 K and 295 K. Thus, more studies on different aromatic precursors and experimental conditions are needed to complete our understanding of the temperature effect on SOA formation from aromatic precursors.

Although temperature is recognized as a major factor governing gas-particle partitioning, most prior studies have mostly focused on the bulk SOA yields or selected classes of compounds (Ahn et al., 2021; Bahrami et al., 2024; John et al., 2018; Rutter and Schauer, 2007; Svendby et al., 2008; Takekawa et al., 2003; Wei et al., 2016; Zhang et al., 2023; Zhou, 2021). While these approaches have advanced the understanding of SOA formation and representation in models, they often lack molecular level resolved resolution. Experimental studies that probe the effect of temperature on the partitioning of individual SOA oxidation products, remain limited and relatively recent (Deng et al., 2021; Fan et al., 2025; Lannuque et al., 2023; Li et al., 2024). Such measurements are particularly important for refining SOA volatility parameterizations under atmospherically relevant cold conditions, such as those occurring during nighttime or wintertime episodes.

The oxidation flow reactor (OFR, Fig. 1) is a type of continuous-flow reactor that uses substantially elevated oxidant levels to rapidly simulate atmospheric oxidation chemistry (Kang et al., 2007; Peng and Jimenez, 2020). Lannuque et al. (2023) have studied the gas-particle partitioning of toluene in a similar OFR system. Experiments carried at 280 K were characterized by

a higher mass loading in the particle phase compared to those at 295 K, as well as a shift in volatility values of oxidation products towards lower volatility values.

Direct measurements of S/IVOCs in real time remains challenging due to their complexity, diversity, and low concentrations. The analytical development of the "CHemical Analysis of aeRosols ONline" (CHARON) inlet coupled with a proton-transfer-reaction-time of flight-mass spectrometry (PTR-ToF-MS) enables alternative online measurements of both gas and particle phases at molecular level (Eichler et al., 2015). It also allows measuring both gas and particle phases with reduced artefacts associated with particle collection and thermal desorption compared to traditional techniques (Peng et al., 2023). Promising applications have been shown in several laboratory and field studies (Lannuque et al., 2023; Müller et al., 2017; Muller et al., 2017; Piel et al., 2021), while its application to gas-particle partitioning investigations is relatively new (Gkatzelis et al., 2018; Lannuque et al., 2023; Peng et al., 2023; Piel et al., 2021).

The aim of the present study is to evaluate gas-particle partitioning of S/IVOCs involved in SOA formation from the photooxidation of AHs in different conditions. For that purpose, the photooxidation of AH compounds was investigated using an online CHARON-PTR-ToF-MS coupled to an oxidation flow reactor. These laboratory experiments aim at 1) identifying the gas and particle phase products of m-xylene and naphthalene at a molecular level; 2) evaluating the partitioning behavior of individual SOA products; and 3) assessing the effect of atmospheric conditions (temperature variation and NO_x/VOC ratio) on this partitioning. Two compounds, m-xylene and naphthalene, are selected, for the following reasons, i) their ubiquity in urban areas (Fang et al., 2021; Wu et al., 2020; Xuan et al., 2021) ii) their known reactivity with OH radicals that is in the same order of magnitude (Calvert et al., 2015), and iii) their SOA formation potential has been previously demonstrated (Chan et al., 2009; Chen et al., 2016, 2021; Kleindienst et al., 2012; Li et al., 2022; Loza et al., 2012; Lu et al., 2024; Ng et al., 2007; Sato et al., 2022; Song et al., 2005, 2007; Srivastava et al., 2022; Takekawa et al., 2003; Ye et al., 2024; Zhang et al., 2019).

2 Methods

2.1 The OFR experimental setup

Photooxidation experiments have been conducted in a 19.3 L cylindrical aerosol oxidation flow reactor (OFR, 153 mm internal diameter, 105 cm length) made up of quartz, vertically oriented, and surrounded by 6 UVB lamps (Helios Italquartz) with a continuous emission spectrum in the 280-350 nm range (λ_{max} = 310 nm, Fig. 1). An external air conditioning unit is connected to the tube allowing temperature control in the range 280-295 K. The gas phase stream consists of humid air, the selected VOC precursor (m-xylene or naphthalene), nitrogen dioxide (NO_2) and hydrogen peroxide (H_2O_2). For humidification, two glass bottles containing milliQ water are bubbled at 0.2-1 L min^{-1} by pure N_2 in order to maintain relative humidity (RH) around 50 % (from 35 % to 65 %, among all experiments). A constant concentration of m-xylene is generated by flowing a constant flow of 0.15 L min^{-1} of N_2 over a permeation tube containing a pure solution (≥ 99 % purity, Sigma Aldrich) placed in an oven and kept at a constant temperature of 308 K. Some solid naphthalene (99% purity, Sigma Aldrich) is kept in an iced water bath

while headspace is flown at 0.1 L min^{-1} by pure N_2 to generate a constant flow of naphthalene in the flow tube. NO_2 is introduced using a cylinder (100 ± 5 ppm in N_2, Linde) and diluted in N_2 using different mass flow controllers to the desired mixing ratios prior to entering the tube (varying from 40 to 340 ppbV), depending on the required VOC/NO_x conditions. A hydrogen peroxide (H_2O_2) solution (50 % in H_2O, stabilized, Sigma Aldrich) is used as a hydroxyl radical (OH) precursor and is constantly introduced in the OFR by bubbling pure N_2 in the solution at a flow of 0.1-0.2 L min^{-1}. For each experiment, the OH radical concentration generated was estimated by fitting the VOC precursor (m-xylene or naphthalene) decay assuming a pseudo first order reaction with OH radicals using temperature-dependent values of the kinetic rate constant as recommended from NIST Kinetics Database. This estimation is also based on the hypothesis that the other reactions with OH do not limit the reaction of the precursor in the first seconds following lamps switching on. The OH radical concentrations range from 2.2 to 5.4 × 10^7 molecules cm^{-3} corresponding approximately to 1.3 and 3 days of atmospheric OH-radical exposure, taking into account a diurnal average hydroxyl radical concentration of 1.5 × 10^6 molecules cm^{-3} (Mao et al., 2009). Due to background contaminations, compounds with *m/z* 61 and below, mainly acetaldehyde, acetic acid, formaldehyde and formic acid, are not considered in further analysis. Monodispersed ammonium sulphate (AS) seeds serve as a pre-existing surface and are generated by nebulizing a 10^{-2} M AS solution (99.5 % purity, Acros Organics) using a TSI atomizer (model 3076), dried through a silica diffusion drier and then size selected in an Aerodynamic Aerosol Classifier (AAC, Cambustion) to generate monodisperse aerosols with an average diameter of 200 nm. The overall input flow is 2.4 L min^{-1} to ensure a residence time in the tube of 8 minutes. In this configuration, particle losses (or its transmissions through the OFR) were estimated by comparing the concentration of seed particles at the inlet and outlet of the OFR, when generating seed at 200 nm electrical mobility diameters. These losses were daily checked prior to each experiment and were in the range 10 ± 5 %. In addition, precursor losses were estimated to be around 5 % for m-xylene and 10-15 % for naphthalene. Losses of gaseous products generated during SOA experiments were not experimentally evaluated. Lannuque et al. (2023) showed, in a toluene SOA experiment, that wall losses introduced a 10-15 % deviation on the SOA yield when considering both precursors and reactions products. For m-xylene, we can reasonably assume lower losses as the residence time is shorter and the flow tube has a larger inner diameter. For naphthalene, it is probable that the wall losses were higher than that of m-xylene.

2.2 Instrumentation and data analysis

Figure 1 shows the schematic of the experimental set-up, where several online instruments are used to characterize gas and particle phase chemical compositions as well as particle number and size distribution.

A commercial Proton Transfer Reaction-Time of Flight-Mass Spectrometer (PTR-Tof-MS 6000X2, Ionicon Analytik GmbH, Innsbruck, Austria) coupled to a "CHemical Analysis of aeRosols ONline" (CHARON) inlet is used to follow online the gas and particle phase chemical composition of the organic fraction. The CHARON inlet has been already described in detail elsewhere (Eichler et al., 2015; Leglise et al., 2019; Müller et al., 2017). Briefly, the sampled air travels through three major sections of the CHARON inlet 1) a gas phase denuder of activated charcoal that strips off gaseous organics; 2) an aerodynamic lens system (ADL) that collimates the subsampled flow and subsequently enriches the particle concentration and 3) a

thermodesorption unit (TD) heated at $T = 150°$ C that vaporizes the particles prior their introduction into the drift tube. The PTR-ToF-MS is used with hydronium ions (H_3O^+) to ionize organic analytes, and operates at a drift tube pressure of 2.6 mbar, a temperature of 120° C, and a voltage of 230 V. This results in an $E/N = 68$ Td (E = electric field, N = Number density of the gas molecules in the drift, 1 Td = 10^{-17} V cm^2 molecule^{-1}). It represents a relatively low E/N compared to classical 120-140 Td reported in most of PTR-ToF-MS studies, as the aim is to minimize the potential fragmentation of parent ions and facilitate the molecular characterization of SOA. The potential higher dependence of the sensitivity to relative humidity variations at such low E/N can be neglected as all experiments were conducted at fixed relative humidity (Pang, 2015; Tani et al., 2003).

Instrument background has been daily performed using pure N_2, while sensitivity and particle enrichment factors (EF) are controlled at the end of the experiments. A blank was conducted prior to each SOA experiment, using the same conditions (H_2O_2 flow, NOx concentration, temperature, humidity, etc.), in the absence of the VOC precursor (either m-xylene or naphthalene). The products formed during these daily blanks were quantified and subtracted to the signal of the following experiment. EF is determined by CHARON calibration using a vanillic acid solution based on the method recommended by Eichler et al. (2015). Instrument sensitivity is evaluated by calculating the transmission curve using a cylinder containing 14 gas standards (benzene, toluene, ethylbenzene, o-, m-, p-xylene, styrene, 1,2,4-trimethyl-, 1,3,5-trimethylbenzene, chloro-, 1,2-dichloro-, 1,3-dichloro-, 1,4-dichloro-, trichloro benzene, each at 100 ± 10%, ppb in N_2, RESTEK) covering a mass range up to m/z 181.

IDA (Ionicon Data Analyzer 2.1.1.4) is used to process data recorded by the PTR-ToF-MS such as mass calibration, peak shape definition, peak identification and integration, rate constant calculation and VOC quantification (Müller et al., 2013). The peaks at m/z 21.022 ($H_3{}^{18}O^+$), m/z 330.847 corresponding to diiodobenzene ($C_6H_5I_2^+$) and its fragment at m/z 203.943 ($C_6H_5I^+$) are used to recalibrate the mass scale (PerMaSCal® internal standard, 1,3-diiodobenzene, T = 55 °C). Molecular formulas composed of C, H, O, N atoms are assigned based on exact mass position, chemical rules (valence of atoms, for example) and isotopic patterns. The molecular formula is used to calculate dipole moments and polarizability as introduced by (Bosque and Sales, 2002) and (Sekimoto et al., 2017), which allows to calculate k-rate constants based on the ion-molecule collision theories (Gioumousis and Stevenson, 1958; Langevin, 1950; Su and Chesnavich, 1982). Concentrations are then estimated based on the rate constant between a proton and each VOC, the experimental transmission of each compound, and the primary ion intensity.

RStudio (RStudio 2023.06.0 Build 421) is used to perform a non-targeted approach for compound selection based on stability periods before and after oxidation. Time intervals are defined for each experiment corresponding to blank (photooxidation without VOC precursor, and HEPA (High-Efficiency Particulate Air) filter for particle phase), reactant (injection of products before the light has been turned on) and products (stable photooxidation), for both gas and particle phases. A Welch t-test is then used to statistically identify ions that are more concentrated than those in the blank. Then, among the selected ions, the products are defined as compounds more concentrated during oxidation period, and the invert for reactants, based also on Welch t-test.

A high-resolution Time-of-Flight Aerosol Mass Spectrometer (HR-ToF-AMS, Tofwerk AG, Aerodyne Inc. USA) is employed for the quantification of the organic and inorganic aerosol fractions (Canagaratna et al., 2007; DeCarlo et al., 2006), with the data recorded by the AMS being analyzed using the software SQUIRREL (ToF-AMS Analysis Toolkit 1.65C). The ionization efficiency (IE) with respect to nitrate anions was 4.58×10^{-8}. It was calculated using nebulized 300 nm mobility diameter ammonium nitrate particles (BFSP software). The relative IE (RIE) of ammonium was 3.45 based on the mass spectrum of ammonium nitrate data from IE calibrations. The RIE of sulphate was determined by comparing the theoretical and the measured concentration of a solution of ammonium nitrate and ammonium sulphate and was determined to be 1.75. For the organic fraction, the default value of 1.4 was used. The AMS data were corrected by collection efficiency (CE) calculated by comparison to the SMPS (Scanning Mobility Particle Sizer, TSI Classifier model 3082, DMA, TSI CPC 3776) volume using densities of 1.7 g cm^{-3} for ammonium sulphate and 1.4 g cm^{-3} for organics. The CE values varied from 0.3 for pure ammonium sulphate particles to 0.7 after SOA formation.

The SMPS is used for measuring particle size distribution and number concentration. Additional instruments account for a chemiluminescent NO_x analyzer (Envitec, model API200E), a pressure sensor (ATM.ECO, STS) and a temperature-humidity probe (HMP9 Vaisala) positioned close the aerosol flow tube outlet, the last two instruments being connected to a data logger (FieldLogger, NOVUS).

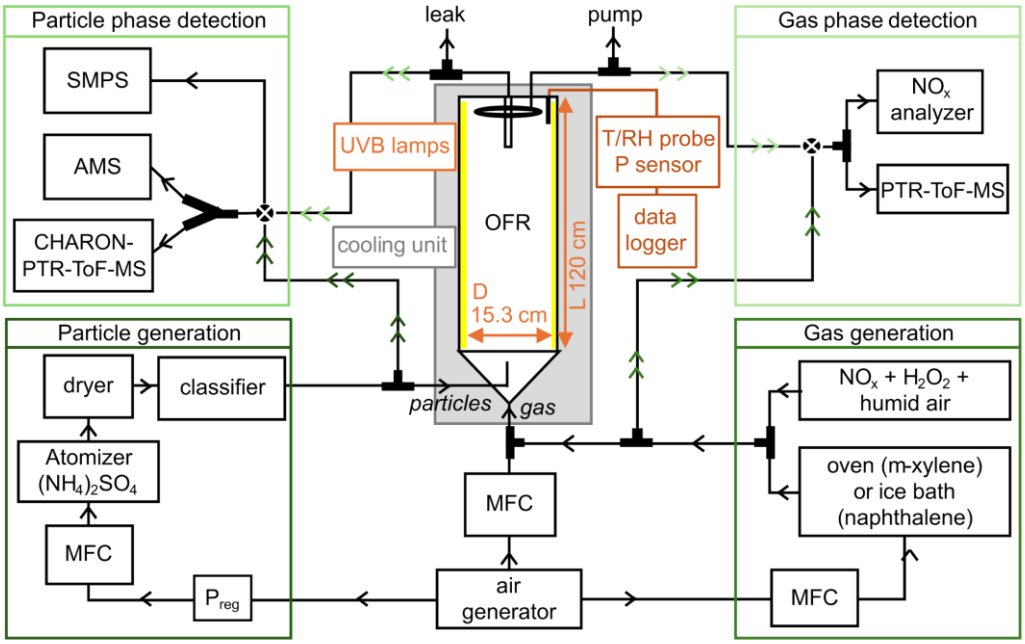

Figure 1. Schematic of the experimental setup. MFC: mass flow controller.

2.3 SOA yield, partitioning, and volatility distribution

The expression to describe the fractional aerosol yield (Y) was established by (Odum et al., 1996, 1997) and is described in Eq. (1), where ΔM_0 is the amount of the total organic aerosol formed (in µg m^{-3}), and ΔVOC is the amount of VOC precursor reacted (in µg m^{-3}) measured as difference between inlet and outlet OFR.

$$Y = \frac{\Delta M_0}{\Delta VOC} \quad (1)$$

The distribution of oxidation products between the gas and particle phases can be explained by the partitioning theory of (Yamasaki et al., 1982):

$$K_{p,i} = \frac{C_{p,i}}{C_{g,i} \times TSP} \quad (2)$$

where $K_{p,i}$ is the experimental partitioning coefficient (in m^3 µg^{-1}) of a species i, $C_{p,i}$ and $C_{g,i}$ are concentrations (in µg m^{-3}) of the species i in particle and gas phases, respectively, as measured by the CHARON-PTR-ToF-MS, and TSP is the total suspended particulate matter of the aerosol (in µg m^{-3}) as measured by SMPS. Larger K_p values indicate a preference for a compound to partition in the particle phase. Subsequently, the volatility of the species can be defined by $\log_{10}C_i^*$, where C_i^* is known as the effective saturation concentration (in µg m^{-3}) of a species i which describes the gas-particle partitioning behavior of organic compounds and represents the gas-phase concentration of a compound at which it will partition equally between the gas and particle phases under given atmospheric conditions, and is calculated as the reciprocal of $K_{p,i}$ (Donahue et al., 2006, 2011):

$$C_i^* = \frac{1}{K_{p,i}} \quad (3)$$

The estimated values have been calculated using the Volcalc model based on molecular properties such as molecular weight, numbers of atoms and functional groups (Meredith et al., 2023; Riemer, 2023). The model is based on SIMPOL.1, a group contribution method (Pankow and Asher, 2008), which implements a structure-activity relationship method to calculate the subcooled pure liquid vapor pressure by summing the contributions of the subcooled liquid vapor pressures of individual chemical functional groups:

$$log_{10}P^{\circ}_{L,i}(T) = \sum_k \nu_{k,i} b_k(T) \quad (4)$$

where $P^{\circ}_{L,i}(T)$ is the liquid vapor pressure (atm), $\nu_{k,i}$ is the number of groups of type k in i, the index k can take on the entire numbers (1,2,3, etc.), and $b_k(T)$ is the group contribution term for group k. No second-order interaction terms are included to account for neighboring functional groups, which means that the model does not consider the potential interactions or effects that adjacent functional groups might have on each other but only sums the contributions of individual functional groups independently.

The saturation concentration ($C^{\circ}_{i,T}$) of the major identified species i is calculated at T = 280 and 295 K as follows:

$$C^{\circ}_{i,T} = C^{\circ}_{i,293} \times \frac{293}{T} \times exp\ exp\left(\left(\frac{-\Delta H}{R}\right) \times \left(\frac{1}{T} - \frac{1}{293}\right)\right) \quad (5)$$

where $C^{\circ}_{i,293}$ is the saturation concentration calculated by Volcalc at T = 293 K, ΔH_i is the enthalpy of vaporization of species i (computationally predicted values from ChemSpider), and R is the ideal gas constant = 8.314 J mol^{-1} K^{-1}.

The saturation concentration (C_i°) and the effective saturation concentration (C_i^{*}) are related through the activity coefficient (γ_i) that captures the non-ideal interactions of the compound with the aerosol mixture. Its value generally lies between 0.3 (readily partitions to particle phase) and 3 (readily partitions to gas phase) for ambient atmospheric aerosol (Donahue et al., 2011; Liu et al., 2021). As in previous studies, such as Isaacman-VanWertz et al. (2016) and Nie et al. (2022), in this work we assume a γ value of 1.

3 Results and discussion

3.1 SOA yield formation

Table 1 summarizes experimental conditions, consumed reactants (ΔVOC) and formed organic aerosol mass (ΔM_0) used to calculate the SOA yield (Y) for each experiment (Eq. (1)). Figure 2 presents SOA yields for (a) m-xylene and (b) naphthalene, comparing them with results from selected previous studies (Chan et al., 2009; Chen et al., 2018; Ng et al., 2007; Song et al., 2005). Filled markers indicate high NO_x conditions (VOC/NO_x < 8), empty markers refer to low NO_x conditions (VOC/NO_x > 8) (Dodge, 1977; NARSTO. and Electric Power Research Institute., 2000). The red square and blue triangle markers refer to this study at 295 K and 280 K, respectively, while all other experiments are conducted at room temperatures (between 295 K and 300 K).

Table 1. List of conducted laboratory experiments and associated conditions, such as OFR temperature, RH, VOC/NO_x ratio, seeds mass and SOA yield.

	T	RH	VOC	NO_x	VOC/NO_x	Seeds	$[OH] \times 10^7$	ΔVOC		ΔM_0	Y
	K	%	ppbV	ppb	ppbC ppb^{-1}	μg m^{-3}	molecules cm^{-3}	μg m^{-3}	%	μg m^{-3}	%
m-xylene	280 ± 1.5	75 ± 5	74 ± 0.65	235	2.5 ± 0.1	51 ± 1.6	3.4 ± 0.5	114 ± 3.3	34	26.4 ± 1.2	23.1 ± 1.2
	280 ± 1.5	50 ± 5	69 ± 0.70	40	13.9 ± 0.5	35 ± 0.5	2.2 ± 0.4	95 ± 3.3	30	26.1 ± 1.9	27.5 ± 2.1
	295 ± 2	60 ± 7	73 ± 0.66	221	2.6 ± 0.1	30 ± 0.8	5.4 ± 0.8	155 ± 3.2	49	12.6 ± 1.4	8.1 ± 1.0
	295 ± 2	55 ± 7	83 ± 0.74	40	16.6 ± 0.6	34 ± 0.7	4.7 ± 0.7	153 ± 3.2	42	21.1 ± 1.4	13.8 ± 1.0
naphthalene	280 ± 1.5	40 ± 3	57 ± 0.35	340	1.7 ± 0.1	46 ± 0.6	2.9 ± 0.2	92 ± 2.3	29	23.3 ± 1.8	25.3 ± 2.0
	280 ± 1.5	35 ± 3	53 ± 0.41	62	9.3 ± 0.4	36 ± 1.0	3.2 ± 0.3	79 ± 2.3	27	33.6 ± 6.9	42.7 ± 8.8
	295 ± 2	40 ± 5	53 ± 0.47	340	1.6 ± 0.1	55 ± 1.5	3.5 ± 0.3	84 ± 2.3	28	12.6 ± 1.7	14.9 ± 2.1

	295 ± 2	50 ± 5	49 ± 0.41	57	8.6 ± 0.4	65 ± 0.3	3.1 ± 0.4	75 ± 2.2	29	13.8 ± 1.6	18.3 ± 2.2

For m-xylene (Fig. 2a), the SOA yield at 295 K under high NOx conditions is approximately 8 % (filled red square), in line with values reported by Ng et al. (2007) and Chen et al. (2018). Chen et al. (2018) reported yields with higher VOC/NO_x ratios, slightly lower precursor concentrations (44-59 ppb), and without using seeds. The absence of seed particles reduces the available surface area for condensation of oxidized products (Lambe et al., 2015). Ng et al. (2007) conducted experiments with AS seeds as in our study, but using nitrous acid (HONO) as OH radical precursor, with varying initial xylene concentrations (from 42 to 171 ppb) which may explain SOA yield variability (from 3 to 8 %). The effect of higher initial levels of the VOC precursor has been shown to reduce aerosol formation (and amount of reacted precursor) and the formation of oxidation products, especially those with m/z > 110 da (Chen et al., 2019). It may be due to the competition between IVOC reactions with OH that produces LVOC/ELVOC, and precursor oxidation. In our case, the initial m-xylene concentration was kept similar between experiments to isolate the effect of temperature and NO_x on SOA yield and chemistry. Both studies by Ng (2007) and Chen (2018) were conducted in dry conditions. Li et al. (2022) reported SOA yields increasing from 6.3 to 14 % when humidity increased from 10 % to 70 %. The order of magnitude of SOA yields in this study is close to what we observed, the variability of yields being associated mostly to NO_x or NH_3 initial concentrations. Under low NO_x, a SOA yield of 14 % (empty red square) is observed, lying on the lower level (12-30 %) of reported values by Song et al. (2007), that used lower levels of xylene (39-52 ppb).

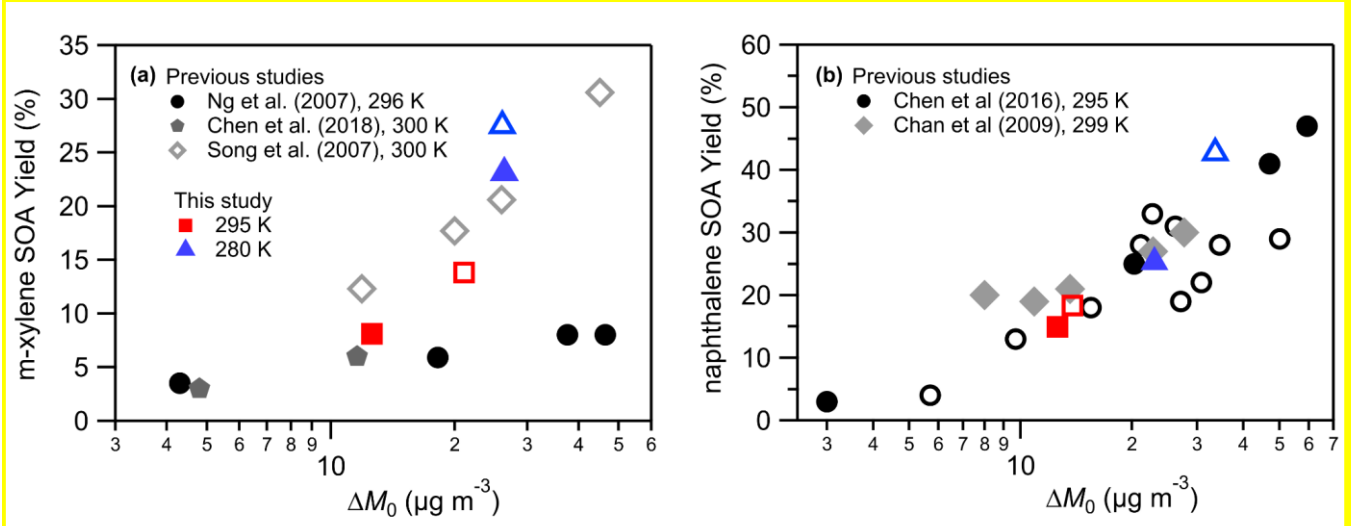

Figure 2. SOA yields at 295 K and 280 K as function of organic aerosol mass formed for (a) m-xylene and (b) naphthalene in comparison with previous studies. Filled markers correspond to high NO_x conditions, open markers to low NO_x.

The effect of temperature on SOA yield is also depicted in Fig. 2. When decreasing from 295 K to 280 K, SOA yield increases from 8 to 23 % under high NO_x conditions and from 14 to 28 % under low NO_x conditions. Only a few studies investigated the role of low temperature on SOA formation from monoaromatic precursors. Regarding xylene, only Takekawa et al. (2003) reported that SOA yield is enhanced by a factor around 2 (from 6 % to 13 %, on average) when temperature decreases from 303 K to 283 K at a VOC/NO_x around 10 (like low NO_x conditions in this study). This is in good agreement with our results, where a decrease of 15 K doubles the SOA yield under low NO_x conditions (Fig. 2). Lannuque et al., (2023) found a similar temperature dependence of toluene-SOA and highlighted that the effect was greater for low concentrations of the precursors.

For naphthalene (Fig. 2b), SOA yield at 295 K with high NO_x conditions ranges from 15 to 18 %, in agreement with Chen et al. (2016) and Chan et al. (2009) that reported values from 3 % to 47 %. Chen et al. (2016) observed the lowest SOA yield under high NO_x, attributed to the lowest amount of OH generated and highest NO injection. Even though Chan et al. (2009) used AS seeds, the initial amount of naphthalene was less than half of that used in our experiments and the humidity was below 10 %, highlighting again the important effect of experimental conditions on the prediction of SOA yields. Lower naphthalene SOA yields are observed under high NO_x conditions (filled vs empty square or triangle, Fig. 2). Under low NO_x conditions, a yield of 18 % is observed in quite good agreement with Chen et al. (2016), who reported yields varying from 4 % to 29 % as a function of the VOC/NO_x ratio, with lowest yields for highest NO_x regimes. A consistent increase in SOA yield is observed when switching from high to low NO_x regime at 280 K, from 25 to 43 % at 280 K, while at 295 K the variation is limited to a few percent increase. The presence of NO_x in the system may promote a competition for the termination reaction of RO_2 radicals between peroxy radicals (RO_2 and HO_2) and NO_x (NO_2 and NO), leading to less oxidized products of higher volatility (Henze et al., 2008; Kroll and Seinfeld, 2008).

The effect of temperature on naphthalene SOA is reported here for the first time. Reducing the temperature from 295 K to 280 K induces an increase from 14.9 % to 25.3 % for high NO_x conditions, and from 18.3 % to 42.7 % for low NO_x conditions. SOA yields from naphthalene are in general higher compared to m-xylene, which is expected considering larger carbon skeleton of naphthalene (Aumont et al., 2013; La et al., 2016), and are in good agreement with previous studies (Chan et al., 2009; Chen et al., 2018). However, the effect of temperature on naphthalene SOA yield is slightly lower compared to the m-xylene SOA system. This may be the result of the larger carbon skeleton of naphthalene, leading to products of lower volatility, that have already partitioned more in the particle phase at 295 K.

3.2 Chemical composition of oxidation products in gas and particle phases

3.2.1 m-xylene

Figure 3 presents the chemical distribution of gas (Figs. 3a,c) and particles (Figs. 3b,d) phase products as a function of the carbon atoms following m-xylene oxidation by OH radicals. The mass fraction (in $\mu g\ m^{-3}$) is further sub-classified based on the number of oxygen (Figs. 3a,b) and nitrogen atoms (Figs. 3c,d; according to color scale), and the molecular weight distribution was divided into three groups: *m*/*z* below 100, *m*/*z* 101-150, and *m*/*z* above 150. The experiment has been carried

out under high NO_x at 280 K. The total m-xylene carbon balance varies within 26-48 % for the detected gas phase products depending on the oxidation conditions and considering that CO, CO_2 and glyoxal are not measured. The latter compound has strong interferences with the high signal of acetone. The SOA formed corresponds to 2.5 % of the total carbon balance at 295 K and 7 % at 280 K under high NO_x conditions.

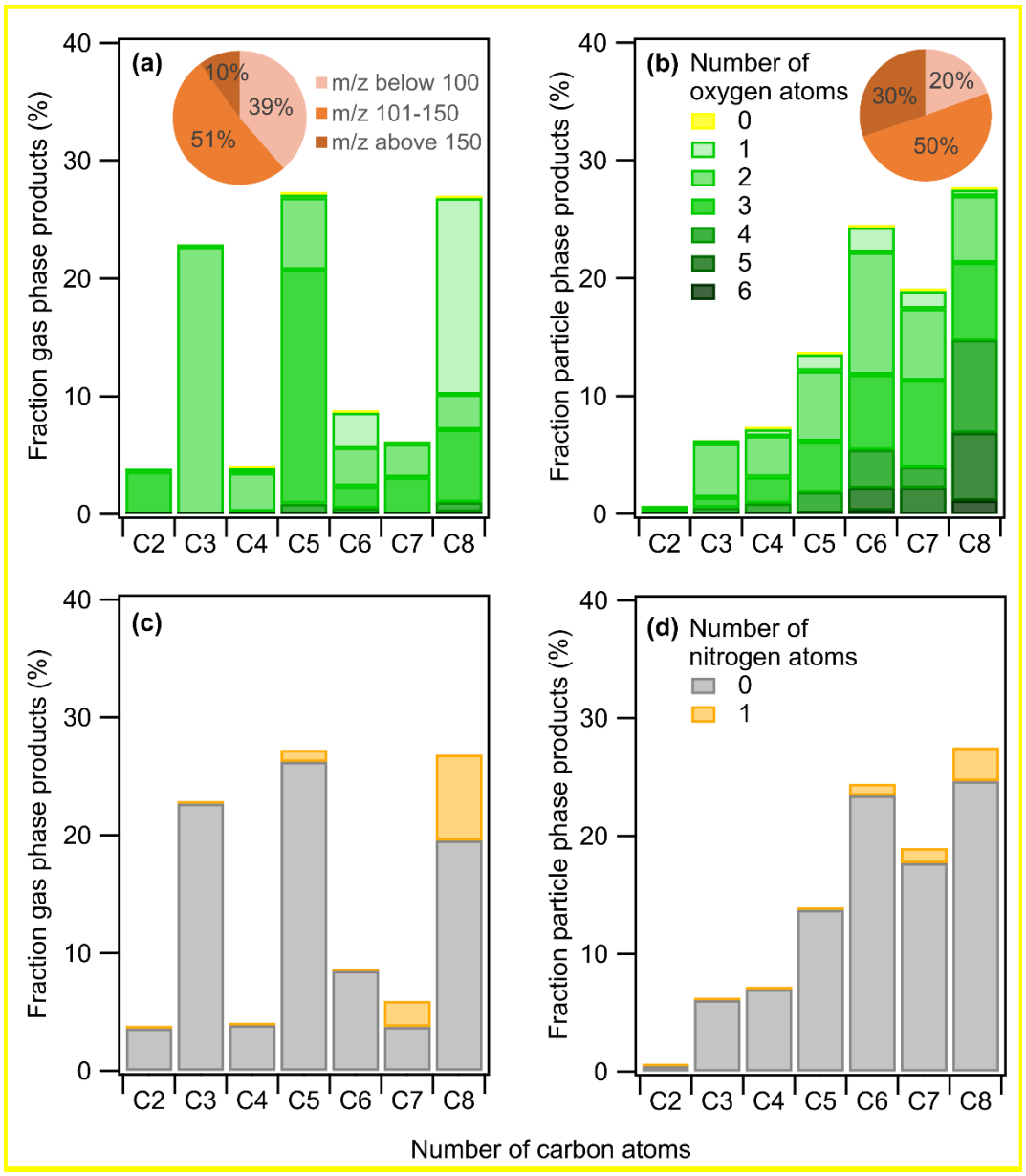

Figure 3. m-xylene mass products fraction (y-axis) distribution based on the number of carbon atoms (x-axis) for a high NO_x experiment at 280 K, colored by the number of (a,b) oxygen and (c,d) nitrogen atoms. Detected compounds are in the (a,c) gas phase and (b,d) particle phase. Pie charts correspond to the molecular weight contribution to the overall mass.

The overall product distribution at 295 K is similar to that at 280 K and can be found in the SI (Figs. S1a and S1b). At both temperatures, the gas phase is mainly composed of C_3, C_5 and C_8 products with 1 to 3 O atoms for most of them, while the particle phase is dominated by C_6, C_7 and C_8 compounds, containing generally 2 to 5 O atoms. In the gas phase, C_8 compounds are ring retaining compounds related to first-generation products, while C_3 and C_5 products arise from a more advanced chemistry. A larger fraction of C_3 products is present in the gas phase at 295 K when compared to 280 K (Figs. 3 and S1a). This could be due to the higher OH concentration for the experiment at 295 K (Table 1), leading to a higher consumption of C_6 and C_8 oxidation products due to their faster reactivity. This is supported by the time evolution of some compounds such as C_6H_8O at *m/z* 97.06, $C_6H_6O_2$ at *m/z* 111.04, $C_6H_8O_4$ at *m/z* 145.05, $C_8H_{10}O_5$ at *m/z* 187.06 (Fig. S3). This hypothesis is also backed up by previous studies reporting the reaction of oxidation products (Cappa and Wilson, 2012; Isaacman-VanWertz et al., 2018; Jin et al., 2021). While for experiments with lower OH concentration, as at 280 K, the gas phase products (Fig. 3a) are characterized by a higher fraction of C_8 (26%) and C_5 (27%) compounds.

The condensed phase is enriched in compounds with higher molecular weight when compared to the gas phase, along with the presence of four or more oxygen atoms which highly reduces their vapor pressure (Cappa and Wilson, 2012). Particle phase products generally exhibit an increasing trend from C_1 to C_8 (Fig. 3b), similar to a recent study on toluene SOA (Lannuque et al., 2023).

The presence of NO_x may affect product distribution, directly through the formation of organic nitrates, or indirectly by playing a role in shaping oxidation chemistry depending on experimental conditions. The comparison of the chemical composition of gas phase products in low NO_x and high NO_x at 295 K showed a general similar distribution (Fig. S1 and S2). The only noticeable change is the stronger contribution of C_3 and C_5 compounds in the low NO_x experiment resulting from the slight increase in OH radical production as described above (Table 1), rather than a real NO_x effect. This is supported by the same product distribution in particle phase, when comparing high and low NO_x, with only a small increase in organic nitrates at high NO_x. The very close distribution between high and low NO_x means that the chemistry was not strongly dependent on the NO_x regime in our conditions, and that NO_x did not significantly affect the oxidant levels in the OFR.

Table 2 lists identified ions from the gas and particle phase products for two experiments at high NO_x at 295 K and 280 K. The columns present the measured *m/z* signals, the attributed chemical formula and a tentative chemical assignment based on results from previous studies on m-xylene photooxidation (Atkinson et al., 1991; Forstner et al., 1997; Huang et al., 2008; Jang and Kamens, 2001; Li et al., 2018, 2022; Zhang et al., 2019a, b; Zhao et al., 2005) and on the CHARON assignment procedure recommended by Gkatzelis et al. (2018) where average saturation mass concentration $\log_{10}(C_i^*)$ are used to discriminate between parent and fragment ions. The compounds are sorted in decreasing numbers of carbon atoms. For each temperature, two columns are presented: the first indicates the contribution of each compound to total gas phase organic products and the second the contribution to SOA.

Table 2. Ions and their corresponding formulas of the major m-xylene products detected during photooxidation experiments under high NO_x. Reaction products are given as a fraction of the gas phase products (in % of µg m^{-3}) and as a fraction of the SOA products (in % of µg m^{-3}).

Carbon number	Measured *m*/*z* and ion sum formula	Tentative assignment	*T* = 298 K		*T* = 280 K	
			Gaseous Products (%)	SOA Products (%)	Gaseous Products (%)	SOA products (%)
8	121.06 $(C_8H_8O)H^+$	m-tolualdehyde	13.9	0.6	16.7	0.5
8	155.07 $(C_8H_{10}O_3)H^+$	dimethyl-epoxy-oxo-hexenal/ trihydroxy dimethyl benzene	n.d.	3.8	n.d.	3.3
8	137.06 $(C_8H_8O_2)H^+$	toluic acid and possible contribution frag. 155.07	n.d.	8.5	n.d.	5.7
8	171.07 $(C_8H_{10}O_4)H^+$	dihydroxy-dimethyl-cyclohexenedione / dimethyl-hexadienedioic acid	0.3	4.6	0.3	5.6
8	153.06 $(C_8H_8O_3)H^+$	hydroxy dimethyl quinone	1.9	2.8	2.4	2.9
8	187.06 $(C_8H_{10}O_5)H^+$	hydroxy-cyclohexene-dicarboxylic acid oxo-cyclohexanedicarboxylic acid	0.1	2.6	0.1	2.5
8	169.05 $(C_8H_8O_4)H^+$	dihydroxy-methylbenzoic acid	n.d.	2.0	n.d.	1.6
8	185.05 $(C_8H_8O_5)H^+$	trihydroxy-(hydroxymethyl)benzaldehyde	n.d.	1.0	n.d.	0.7
8	168.06 $(C_8H_9NO_3)H^+$	*dimethyl nitrophenol*	1.9	0.4	3.6	0.4
8	152.07 $(C_8H_9NO_2)H^+$	*nitro-xylene*	0.4	0.1	1.8	0.1
7	125.06 $(C_7H_8O_2)H^+$	dimethyl-pyranone/ methyl-hexadienedial	n.d.	3.6	1.6	5.0
7	141.05 $(C_7H_8O_3)H^+$	methyl-oxo-hexadienoic acid /heptenetrione	0.7	2.8	0.7	4.0
7	139.04 $(C_7H_6O_3)H^+$	hydroxy benzoic acid/ hydroxy methyl benzoquinone	n.d.	3.1	n.d.	2.4
7	157.05 $(C_7H_8O_4)H^+$	hydroxy-dioxo-heptenal / epoxymethylhexenedial	n.d.	2.0	n.d.	1.8
7	109.06 $(C_7H_8O)H^+$	cresols/ benzyl alcohol	n.d.	1.4	n.d.	1.5
7	173.06 $(C_7H_8O_5)H^+$	hydroxy-dioxo-heptenoic acid	n.d.	1.8	n.d.	1.2
7	138.06 $(C_7H_7NO_2)H^+$	*nitrotoluene*	1.1	0.4	1.2	0.3
7	154.05 $(C_7H_7NO_3)H^+$	*nitrocresol*	0.7	0.3	0.6	0.3
6	127.04 $(C_6H_6O_3)H^+$	hydroxymethyl furfural/ hydroxyquinol/dimethylfurandione	1.0	2.4	1.4	3.3
6	113.06 $(C_6H_8O_2)H^+$	methyl-oxo-pentenal / dimethylfuranone	n.d.	1.7	0.2	2.2
6	129.06 $(C_6H_8O_3)H^+$	hydroxy-oxo-hexenal methyl-oxo-pentenoic acid	0.4	1.6	0.4	2.7
6	111.04 $(C_6H_6O_2)H^+$	methylfuraldehyde / benzenediols possible frag. of 129.06	n.d.	3.6	2.7	6.2
6	143.03 $(C_6H_6O_4)H^+$	dioxo-hexenoic acid/ methyl-dioxo-pentenoic acid tetrahydroxybenzene	n.d.	1.4	0.2	1.8
6	159.04 $(C_6H_6O_5)H^+$	oxo-hexenedioic acid	n.d.	1.2	n.d.	1.2
6	145.05 $(C_6H_8O_4)H^+$	hydroxy-dioxo hexanal	n.d.	1.2	0.1	1.1
6	115.07 $(C_6H_{10}O_2)H^+$	cyclopentylcarboxylic acid	n.d.	0.4	0.4	1.1
6	95.03 $(C_6H_6O)H^+$	phenol	n.d.	1.4	n.d.	1.2
5	113.02 $(C_5H_4O_3)H^+$	methyl-furandione	16.7	1.3	19.3	2.1

5	131.04 $(C_5H_6O_4)H^+$	methy-hydroxy-oxo-butandial	2.1	1.4	0.9	0.9
5	117.05 $(C_5H_8O_3)H^+$	oxo-pentanoic acid + frag at 99.04	1.2	0.7	0.2	0.4
	99.04 $(C_5H_6O_2)H^+$	oxo-pentenal / methyl-butendial	6.7	3.5	2.8	3.9
5	115.03 $(C_5H_6O_3)H^+$	oxo-pentenoic acid	1.4	2.4	0.7	1.8
5	97.03 $(C_5H_4O_2)H^+$	furaldehyde	1.1	0.7	2.2	1.7
5	101.06 $(C_5H_8O_2)H^+$	oxo-pentanal and isomers + frag at 83.05	n.d	0.4	n.d	0.4
	83.05 $(C_5H_6O)H^+$	methylfuran	0.6	1.0	0.3	1.3
4	71.05 $(C_4H_6O)H^+$	dihydrofuran / MACR / MVK	1.1	0.3	0.4	0.3
4	87.04 $(C_4H_6O_2)H^+$	butanedial / crotonic acid	n.d.	2.0	n.d.	2.2
4	103.04 $(C_4H_6O_3)H^+$	hydroxy-oxo-butanal	0.4	1.5	0.1	1.3
4	85.03 $(C_4H_4O_2)H^+$	butenedial	n.d.	1.3	n.d.	1.2
3	73.03 $(C_3H_4O_2)H^+$	methylglyoxal	20.9	3.2	9.5	2.7
3	75.04 $(C_3H_6O_2)H^+$	propanoic acid	14.3	1.7	13.3	1.6
3	89.02 $(C_3H_4O_3)H^+$	pyruvic acid / hydroxy-propanedial	1.5	0.6	n.d.	0.6
2	77.03 $(C_2H_4O_3)H^+$	PAN fragment	3.7	0.3	3.6	0.5

*n.d. = not detected

The C_8 compounds are dominating both gas and particle phases accounting for 27 % of the total products. The most abundant C_8 gas phase product is m-tolualdehyde (C_8H_8O detected at *m*/*z* 121.06), comprising alone 17 % of the reaction products. It is a first generation ring-retaining aromatic compound previously identified in many studies (Atkinson et al., 1991; Forstner et al., 1997; Huang et al., 2008; Srivastava et al., 2023; Zhang et al., 2019b; Zhao et al., 2005). Toluic acid is a second generation ring retaining compound formed by the additional oxidation of m-tolualdehyde by OH radical (Forstner et al., 1997; Srivastava et al., 2022, 2023), and it is a major C_8 particle phase product ($C_8H_8O_2$, detected at *m*/*z* 137.06) contributing to 5 % of the SOA mass. Another major SOA component is found at *m*/*z* 171.07 ($C_8H_{10}O_4$) tentatively assigned to dimethyl-hexadienedioic acid, a ring opening product possibly formed by OH-addition to the benzene ring followed by a ring cleavage, or to dihydroxy-dimethyl-cyclohexenedione, a ring retaining compound formed by successive OH radical reactions on the benzene ring. A second ring opening compound is detected at *m*/*z* 155.07 ($C_8H_{10}O_3$) previously identified as dimethyl-epoxy-oxo-hexenal (Zhao et al., 2005). Other C_8 compounds are $C_8H_8O_{3\text{-}5}$ (at *m*/*z* 153.06, *m*/*z* 169.05 and *m*/*z* 185.05) and $C_8H_{10}O_5$ at *m*/*z* 187.06 (Table 2).

The contribution of C_7 compounds to gas and particle phases accounts for 6 % and 19 %, respectively. Among the C_7 prominent products in the particle phase we identify $C_7H_8O_2$ at *m*/*z* 125.06 tentatively assigned to dimethyl-pyranone (Forstner et al., 1997) or methyl-hexadienedial resulting from a ring opening of the phenoxy radical intermediate formed via OH-addition to the ring (Jang and Kamens, 2001). Further oxidation of methyl-hexadienedial will result in methyl-oxo-hexadienoic acid $C_7H_8O_3$ at *m*/*z* 141.05 (Jang and Kamens, 2001). Another C_7 compound is the $C_7H_6O_3$ at *m*/*z* 139.04 tentatively assigned to methyl cyclohexene tricarbonyls or hydroxy methyl benzoquinone, both being ring-retaining products. They can be formed upon OH-addition to first- or second-generation products and release of one methyl group (Jang and Kamens, 2001). Other C_7

compounds important in the particle phase include C_7H_8O (detected at *m/z* 109.06), $C_7H_8O_4$ (detected at *m/z* 157.05), and $C_7H_8O_5$ (detected at *m/z* 173.04). Some of the C_7-C_8 products are nitrogen containing-compounds: nitro-m-xylene ($C_8H_9NO_2$, at *m/z* 152.07), nitrotoluene ($C_7H_7NO_2$ at *m/z* 138.06), dimethyl nitrophenol ($C_8H_9NO_3$ at *m/z* 168.06) and nitrocresol ($C_7H_7NO_3$ at *m/z* 154.05). The latter is the result of NO_2 reaction with the benzyl peroxy radical in the H-abstraction route (Li et al., 2018; Srivastava et al., 2023). Aliphatic nitrogen-containing compounds are easily fragmented in the PTR-MS and thus are hardly detected. Nevertheless, a known peroxyacetyl nitrate (PAN) fragment $C_2H_4O_3$ detected at *m/z* 77.03, also previously assigned as an unspecific fragment from nitro-group containing compounds has been detected (Müller et al., 2012). In total, the sum of all nitrogen-containing products (including PAN fragment) accounted for 9-14 % of the gaseous phase mass loading and 6 % of the particulate phase under high-NO_x conditions, which is close to what was seen in toluene photooxidation experiments by Lannuque et al. (2023). Under low NO_x conditions, organic nitrates (including PAN fragment) accounted for 4-12 % in the gas phase and 3-4 % in the particle phase out of total products, indicating limited NO_x influence on the formation of nitrogen-containing compounds (Figs. S1c,d; S2c,d). These results suggest that in our system, the shift from low to high NO_x did not substantially alter the oxidation pathways or enhance NO_x-dependent products formation.

The C_6 compounds accounted for only 6 % of the gas phase and for 19% of the organic aerosol fraction. Top products are ring-retaining furan-derived, such as methyl-furaldehyde or benzenediols ($C_6H_6O_2$, detected at *m/z* 111.04) making up 3 % and 6 % in gas and particle phases respectively, and dimethylfurandione ($C_6H_6O_3$, detected at *m/z* 127.04) with 1.4 % in the gas phase, and 3.3 % in the particle phase, alongside with dimethyl-furanone with 2.2 % in the particle phase ($C_6H_8O_2$, detected at *m/z* 113.06). Furanoid products can be formed through a bridged oxide intermediate on a bicyclic ring whereas furandiones are known to originate from conjugated dicarbonyls via reaction with OH-radicals followed by cyclization (Forstner et al., 1997; Jang and Kamens, 2001). Examples of unsaturated dicarbonyls and tricarbonyls in the condensed phase are methyl-oxo-pentenal ($C_6H_8O_2$, detected at *m/z* 113.06), and hydroxy-oxo-hexenal ($C_6H_8O_3$, detected at *m/z* 129.06), also assigned to methyl-oxo-pentenoic acid (Li et al., 2017, 2018; Zhao et al., 2005). Those multi-carbonyls are a result of the decomposition of bicyclic alkoxy radicals (Huang et al., 2008; Zhao et al., 2005). Other C_6 compounds can be found at m/z 143.03 ($C_6H_6O_4$), 97.06 (C_6H_8O), 145.05 ($C_6H_8O_4$), and 115.07 ($C_6H_{10}O_2$) (Table 2).

As shown in Fig. 3 and Fig. S1, the C_5 products represent a major contributor of the gas phase with around 30 % of the total organic gaseous products and 13 % of the particle phase. In agreement with previous studies, most of the compounds are furan derivatives (Forstner et al., 1997; Jang and Kamens, 2001; Li et al., 2018). The $C_5H_4O_3$ (detected at *m/z* 113.02) assigned to methylfurandione accounts alone for, 17-19 % of the gas phase products, followed by oxo-pentenal and isomers ($C_5H_6O_2$, detected at *m/z* 99.04) with 3-7 % abundance. Other important products include unsaturated or oxo-aldehydes (such as $C_5H_6O_2$ at *m/z* 99.04 and $C_5H_6O_4$ at *m/z* 131.04), organic acids such oxo-pentenoic acid ($C_5H_6O_3$ at *m/z* 115.03) (Table 2). Lannuque et al. (2023) identified dihydroxy-oxopentanoic acid (DHOPA, $C_5H_8O_5$), a known tracer of toluene and xylene SOA, in particle phase. In our study, DHOPA parent ion was below the detection limit which is highly probable considering its very low formation yield (Srivastava et al., 2023) and the low precursor concentration used compared to Lannuque et al. (2023). We therefore assume that DHOPA did not contribute significantly to the fragment ion at *m/z* 131.04 ($C_5H_6O_4$) expected upon water

loss. In general the high contribution of C_5 compounds can be explained by the m-xylene structure (C_8 aromatic) and the presence of two methyl groups on the benzene ring, which implies the formation of methylated furan derivates such as methyl-furandione, methyl-furanone and furaldehyde, in addition to the high contribution of C_3 compounds such as methylglyoxal, in agreement with previous studies (Birdsall and Elrod, 2011; Fan and Zhang, 2008; Forstner et al., 1997; Jang and Kamens, 2001; Li et al., 2022; Song et al., 2007; Zhang et al., 2019b).

The C_4 compounds are the least abundant in both phases (below 7 %, on average) and account for shorter functionalized aldehydes, furans and acids formed by minor pathways in the aromatic ring cleavage (Table 2). This is in agreement with the above explained ring opening mechanism, that mainly breaks the carbon skeleton of the xylene in C_5 and C_3 compounds, instead of two C_4 moieties (Forstner et al., 1997; Jenkin et al., 2003; Pan and Wang, 2014).

The C_3 compounds account for 23-37 % of the gas phase and 6 % of the particle phase products. Methylglyoxal ($C_3H_4O_2$, detected at *m*/*z* 73.03) accounts for 21% of the gas phase products at 295 K while it is close to 10 % at 280 K. It makes up to 3 % of the SOA fraction and is a major second-generation product resulting from the ring cleavage of bicyclic alkoxy radicals (Fan and Zhang, 2008). Propanoic acid ($C_3H_6O_2$, detected at *m*/*z* 75.04) accounts for 8 % of the gaseous phase and only 1 % in the particle phase, as it is a quite volatile compound. This reaction product can result from the oxidation of multifunctional ring opening products (Jang and Kamens, 2001).

3.2.2 Naphthalene

In analogy with the m-xylene, Fig. 4 presents the chemical distribution of naphthalene gas phase products (Figs. 4a,c) and particle phase products (Figs. 4b,d) for photooxidation experiments under high NO_x conditions at 280 K, in addition to pie charts showing the molecular weight distribution. Out of the total naphthalene carbon balance, 30-32 % is accounted for the detected gas phase products under the different oxidation conditions, taking into account that CO, CO_2 and glyoxal are not measured. As for the SOA formed, it corresponds to 8 % at 295 K and 14 % at 280 K of the carbon balance under high NO_x conditions.

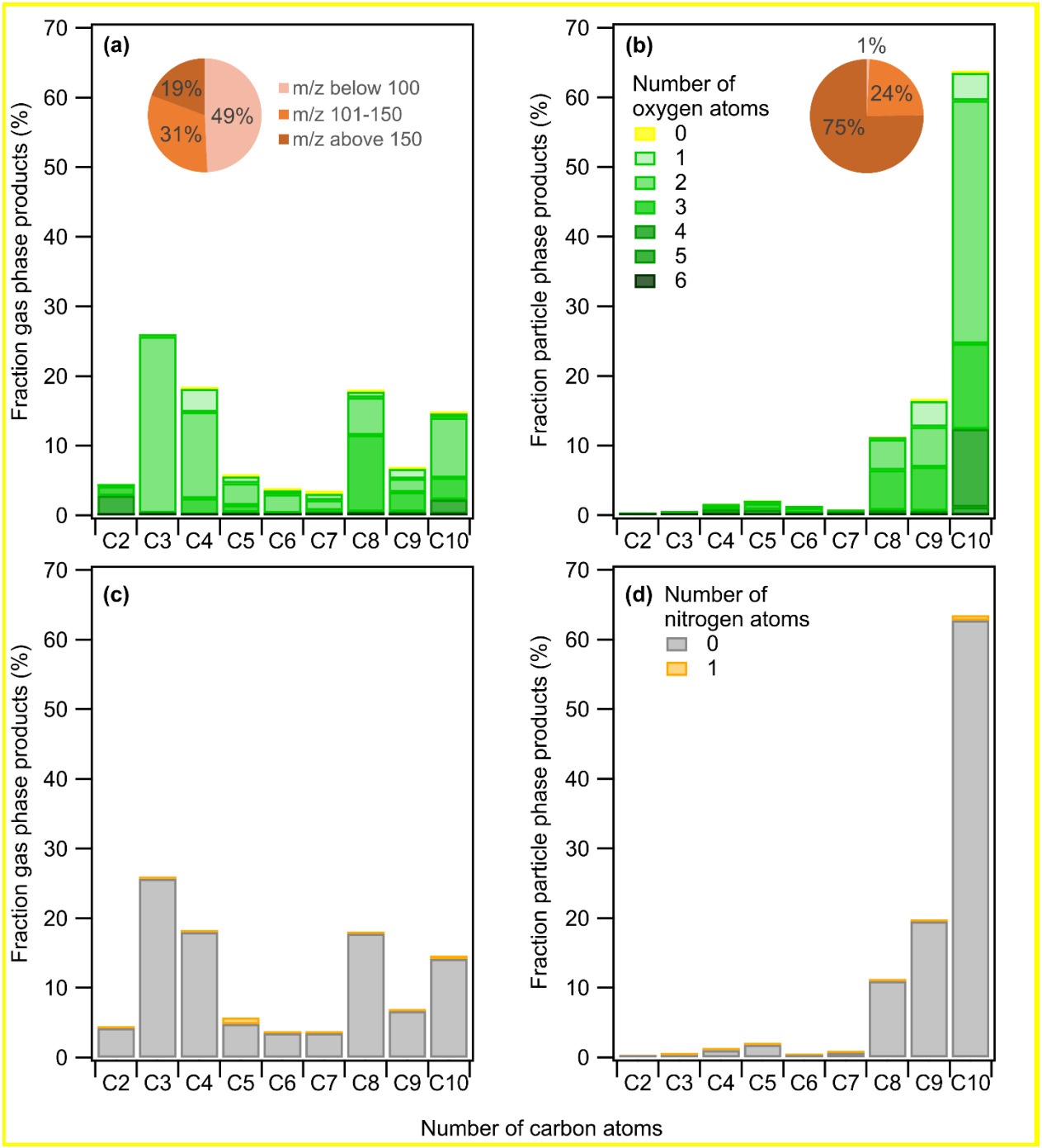

Figure 4. Naphthalene mass products fraction (y-axis) distribution based on the number of carbon atoms (x-axis) for a high NO_x experiment at 280 K, colored by the number of (a,b) oxygen and (c,d) nitrogen atoms. Detected compounds are in the (a,c) gas phase and (b,d) particle phase. Pie charts correspond to the molecular weight contribution to the overall mass.

As the measured carbon distribution is comparable at the two temperature conditions, only the experiment at 280 K is shown in the main text (see Fig. S2 for distributions at 295 K). The gas phase products distribution is dominated by C_{10} and C_8 compounds containing mainly 2 or 3 oxygen atoms followed by C_3 and C_4 compounds, such as methylglyoxal, resulting from the further degradation of naphthalene oxidation products. As expected, the particle phase contains more oxygen atoms and is characterized by heavy molecular weight compounds with *m/z* above 150 comprising 75 % of the overall mass, explained by the readily partitioning of major C_{10} products containing mainly 2 to 4 oxygen atoms. Table 3 presents the major identified ion fragments, their corresponding chemical formula and a tentative assignment to each compound based on previous studies (Bunce et al., 1997; Chan et al., 2009; Chen et al., 2016; Kautzman et al., 2010; Lee and Lane, 2009; Nishino et al., 2009; Riva, 2013; Sasaki et al., 1997; Tomaz, 2015). Similar to what was observed in the case of m-xylene, the overall oxidation product distributions, including nitrogenous species (1-4 % in both high and low NO_x conditions), remain comparable across NO_x conditions (Figs. S4 and S5 at 295 K). The strong similarity in product distributions and molecular compositions implies minimal shifts in bulk volatility as well in oxidation conditions.

Table 3. List of ions and their corresponding formulas of the major naphthalene products detected during photooxidation experiments under high NO_x. Reaction products are given as a fraction of the gas phase products (in % of µg m^{-3}) and as a fraction of the SOA products (in % of µg m^{-3}).

Carbon number	Measured *m/z* and ion sum formula	Tentative assignment	*T* = 295 K		*T* = 280 K	
			Gaseous products (%)	SOA products (%)	Gaseous products (%)	SOA products (%)
10	161.06 $(C_{10}H_8O_2)H^+$	formyl cinnamaldehyde	2.0	8.9	3.5	25.4
10	193.05 $(C_{10}H_8O_4)H^+$	carboxy cinnamic acid	0.8	15.3	1.0	8.1
10	159.04 $(C_{10}H_6O_2)H^+$	naphthoquinone	6.6	5.6	4.9	9.3
10	177.05 $(C_{10}H_8O_3)H^+$	formyl cinnamic acid	0.6	7.7	1.1	7.1
10	175.04 $(C_{10}H_6O_3)H^+$	epoxy-naphthoquinone	1.6	8.4	1.9	4.8
10	145.07 $(C_{10}H_8O)H^+$	naphthol	0.4	2.2	0.5	3.6
10	191.04 $(C_{10}H_6O_4)H^+$	dihydroxy naphthoquinone	0.7	3.5	0.8	2.0
10	195.06 $(C_{10}H_{10}O_4)H^+$	carboxybenzenepropanoic acid benzofurancarboxyaldehyde	0.3	1.5	0.3	1.0
10	174.05 $(C_{10}H_7NO_2)H^+$	*nitronaphthalene*	1.2	0.3	0.3	0.2
10	190.05 $(C_{10}H_7NO_3)H^+$	*nitronaphthol*	0.5	2.5	0.1	0.4
9	147.05 $(C_9H_6O_2)H^+$	benzopyrone	3.5	8.3	1.9	5.8
9	163.04 $(C_9H_6O_3)H^+$	hydroxycoumarin	1.5	6.3	2.2	4.5
9	133.06 $(C_9H_8O)H^+$	indanone	1.6	1.3	1.3	3.6
9	179.04 $(C_9H_6O_4)H^+$	dihydroxy-indanedione	0.5	4.2	0.1	2.8
9	165.06 $(C_9H_8O_3)H^+$	hydroxy cinnamic acid	0.9	2.7	0.6	1.8
9	181.05 $(C_9H_8O_4)H^+$	dihydroxy cinnamic acid	0.2	1.5	0.2	0.9
8	135.05 $(C_8H_6O_2)H^+$	phthaldialdehyde / phthalide	19.3	3.9	5.4	4.3
8	149.03 $(C_8H_4O_3)H^+$	phthalic anhydride	13.8	3.3	9.9	2.0

8	151.04 $(C_8H_6O_3)H^+$	hydroxy phthaldehyde hydroxy phthalide	0.5	1.2	1.0	3.7
7	123.05 $(C_7H_6O)H^+$	benzoic acid	1.9	0.2	1.4	0.1
7	107.05 $(C_7H_6O)H^+$	benzaldehyde	1.0	n.d.	0.9	n.d.
6	111.05 $(C_6H_6O_2)H^+$	catechol / benzoquinone	1.2	n.d.	0.9	n.d.
6	115.07 $(C_6H_{10}O_2)H^+$	dimethyloxolan-one / hexanedione	1.3	0.3	1.3	0.6
5	101.06 $(C_5H_8O_2)H^+$	methyl furan	0.7	n.d.	1.6	n.d.
4	89.06 $(C_4H_8O_2)H^+$	hydroxybutanone / hydroxybutanal	10.1	0.1	11.5	n.d.
4	71.05 $(C_4H_6O)H^+$	dihydrofuran / MACR / MVK	1.2	n.d.	1.8	n.d.
3	75.04 $(C_3H_6O_2)H^+$	propanoic acid	12.3	0.3	19.9	0.2
3	73.03 $(C_3H_4O_2)H^+$	methylglyoxal	3.6	0.1	5.4	0.1
2	77.02 $(C_2H_4O_3)H^+$	PAN fragment	2.0	0.1	1.3	0.1

*n.d. = not detected

The C_{10} compounds account for around 15 % of the gas phase products at both temperatures and clearly dominate the particulate phase with 59 % and 64 % of the overall aerosol mass at 295 K and 280 K, respectively. The 2-formyl cinnamaldehyde ($C_{10}H_8O_2$ at *m/z* 161.06) is the most abundant particle phase product accounts for 25 % of the SOA formed at 280 K. It is assumed to be formed via two possible routes i) ring cleavage upon the reaction of the naphthol peroxy radical (from an OH-naphthalene adduct) with NO, and ii) a hydrogen shift from the alcohol group on the naphthol peroxy radical followed by loss of OH and ring opening (Kautzman et al., 2010; Nishino et al., 2009; Qu et al., 2006; Sasaki et al., 1997; Wang et al., 2007). The predominance of one route over the other is depending on the amount of NO_x. The 2-formyl cinnamaldehyde can further be oxidized, leading to the formation of 2-carboxy cinnamic acid ($C_{10}H_8O_4$ at m/z 193.05), the second most important C_{10} compound that accounts for 8-15 % of the SOA mass. The oxidation of 2-formyl cinnamaldehyde also produces 2-formyl cinnamic acid ($C_{10}H_8O_3$ at *m/z* 177.05) (Bunce et al., 1997), that accounts for 7-8 % of the condensed phase. The addition of O_2 to the OH-naphthalene adduct results in the formation of epoxy-quinone ($C_{10}H_6O_3$ at *m/z* 175.04), representing 5-8 % of the particle phase. Other important C_{10} ring retaining compounds are dihydroxy naphthoquinone ($C_{10}H_6O_4$ at *m/z* 191.04) and 1,4-naphthoquinone ($C_{10}H_6O_2$ at m/z 159.04). This latter has multiple formation routes, either from reaction of OH radical with naphthalene or with naphthol ($C_{10}H_8O$ at *m/z* 145.07), or from the photodegradation of nitronaphthalene ($C_{10}H_7NO_2$ at *m/z* 174.05) (Atkinson et al., 1989; Kautzman et al., 2010), potentially explaining the low abundance of the latter (< 1 % in mass) alongside with its reaction product with OH, nitro-naphthol ($C_{10}H_7NO_3$ at *m/z* 190.05). At both high and low NO_x conditions, the NO_2^+ signal in the particle phase did not exceed 3 % out of the aerosol mass detected by CHARON-PTR-ToF-MS meaning that the nitro-derivates of naphthalene did not undergo strong fragmentation. In total, the sum of all nitrogen-containing products (including PAN fragment) accounted for 2-3 % of the gaseous phase mass loading and 1-4 % of the particulate phase under high-NO_x conditions. The observed low yields of nitro derivatives during the photo oxidation of naphthalene is in agreement with previous studies (Kautzman et al., 2010; Lee and Lane, 2009; Sasaki et al., 1997). Nitronaphthol ($C_{10}H_7NO_3$ at m/z 190.05) is a well known tracer of naphthalene SOA in high NO_x conditions, and has been

observed here as a main nitrogen containing compound. Other previously reported tracers (nitrosalicylic acid, dinitrosalicylic acid or nitrophthalic acid) are not detected by CHARON-PTR-ToF-MS. The NO_x conditions in our study might explain they are not formed, since the formation of these compounds is NO_x dependent, and our study used lower NO_x levels compared to studies using HONO or CH_3NO as OH radical precursors, for example (Sato et al., 2022). It should also be considered that the UV lights used, which peaked at 310 nm, may induce photolysis of nitronaphthalene and other nitro-derivates, as previously reported in chamber experiments with similar UV lamps (Healy et al., 2012).

The formation of C_9 and C_7 products can be explained by H-abstraction of 2-formyl cinnamaldehyde, leading to a formyl peroxy radical that subsequently reacts with NO to form an alkoxy radical implying the loss of CO_2 group (Kautzman et al., 2010). The C_9 compounds contribute by 6-9 % to the gas phase and are the second highest contributors to the particle phase with 16-20 % of the total organic mass. Identified chemical formulas include $C_9H_6O_2$ (at *m/z* 147.05) which can be either benzopyrone (also known as coumarin) or indene-dione, as well as indanone (C_9H_8O at *m/z* 133.06) first detected by Lee and Lane (2009). No formation mechanism has been proposed for these products so far, but their molecular structure clearly indicates a rearrangement following ring opening, to form either a new ring at 6 atoms including one oxygen in the case of coumarin, or at 5 atoms for the indene-dione and indanone. This ring closure is a common feature in the case of dialdehydes oxidation, as explained by Lannuque and Sartelet (2024), which may support the hypothesis that these compounds originated from 2-formyl cinnamaldehyde. Further photo-oxidation of coumarin may lead to hydroxycoumarin ($C_9H_6O_3$ at *m/z* 163.04) accounting for 2.2 % of the gas phase and 4-6 % of the particle phase. A more oxygenated compound, dihydroxy-indanedione ($C_9H_6O_4$ at *m/z* 179.04), was previously identified by Lee et al. (2018). Logically, this compound was mainly present in the condensed phase with 3-4 % of the total SOA mass.

C_8 oxidation products make up a good 18-35 % and 10-11 % of the gas and particle phases, respectively. Phthaldialdehyde and phthalic anhydride largely dominate the C_8 compounds and are of particular importance in the gas phase. Phthaldialdehyde ($C_8H_6O_2$ at *m/z* 135.05), is both a first- and second-generation ring-opening product of the OH radical reaction with naphthalene, with the second-generation pathway expected to originate from the reaction of OH radical with 2-formyl cinnamaldehyde (Sasaki et al., 1997; Wang et al., 2007). Further addition of OH radical to phthaldialdehyde will lead to hydroxy phthaldehyde / hydroxy phthalide ($C_8H_6O_3$ at *m/z* 151.04) that makes up 3.7 % of SOA (Table 3), while the H-abstraction followed by intramolecular cyclization results in phthalic anhydride ($C_8H_4O_3$ at m/z 149.03) making up 2-3% of the condensed phase, and 10-14 % in gas phase (Table 3) previously observed by Wang et al. (2007).

C_7 compounds are relatively less abundant accounting for 3 % of the gas phase products and less than 1 % of SOA. They include compounds like benzoic acid ($C_7H_6O_2$ at *m/z* 123.05) and benzaldehyde (C_7H_6O at *m/z* 107.05).

Only two C_6 compounds are detected and represent 3-4 % of the total gas products and only 1 % of the SOA yield. The dominant C_6 in the gaseous phase is $C_6H_{10}O_2$ (at *m/z* 115.07) with 1.3 %, which can be dimethyloxolanone or hexanedione. The former can be formed from the oxidation of phthaldialdehyde, implying the opening of the second aromatic cycle (Kautzman et al., 2010). Another minor C_6 compound is catechol or benzoquinone ($C_6H_{10}O_2$ at *m/z* 115.07).

C_5 products account for only 3-6 % of the gaseous phase and less than 2 % of SOA. A major detected compound is $C_5H_8O_2$ at *m/z* 101.06 (1.6 %) which can be assigned as methyl furan or 4-oxopentanal.

The C_2-C_4 products are more volatile, all together make less than 2 % of the total SOA mass but present a considerable fraction of the gas phase products with 18 % for C_4, 26 % for C_3, and 4 % for C_2. The major C_4 contributor is $C_4H_8O_2$ (at *m/z* 89.06) representing 12 % of the gas phase products. It is tentatively assigned to hydroxybutanal or butanoic acid. Almost all the C_3 fraction is represented by propanoic acid ($C_3H_6O_2$ at *m/z* 75.04) with 12-20 % contribution to the gas phase products, and methylglyoxal ($C_3H_4O_2$ at *m/z* 73.03) up to 5 %. The C_2 compound is tentatively assigned to the PAN fragment $C_2H_4O_3$ detected at *m/z* 77.02 (1.4 %) (Müller et al., 2012).

3.3 Experimentally derived and estimated gas-particle phase partitioning

A two-dimensional space, the 2D-VBS framework (Donahue et al., 2011; Murphy et al., 2012), is used as a means to visualize the compounds distribution as function of the experimentally derived volatility ($\log_{10}C_i^*$) and the O/C ratio (Fig. 5) or the oxidation state of carbon (OSc) (Fig. S4). Such molecular level effect of temperature on SOA for m-xylene and naphthalene is reported here for the first time. Figures 5a and 5b display the distribution of measured volatilities for the major compounds detected in both gas and particle phases for m-xylene and naphthalene, respectively, under high NO_x conditions. The volatilities of the identified compounds are in the range of SVOCs with C_i^* values ranging from 0.3 to 300 µg m^{-3} (vapor pressures approximately 10^{-8} to 10^{-5} torr) to IVOCs with C_i^* values ranging from 300 to 3×10^6 µg m^{-3} (vapor pressures approximately 10^{-5} to 10^{-1} torr) (Donahue et al., 2012), indicated by the light green ($\log_{10}C_i^*$ from 0 to 2.5) and light blue ($\log_{10}C_i^*$ from 2.5 to 5) background shading, respectively. Data points are indicated for the experiments at 280 K (purple circles) and 295 K (red circles), and the size of the circles is proportional to the mass concentration (in µg m^{-3}) of each ion in the particle phase.

For m-xylene approximately out of 110 ions detected in the particle phase, half of them are exclusively found in the particle phase. This fraction should populate a low volatility area (as ELVOC), and it is not represented in this 2D-VBS (Fig.5a) but represents more than 30 % of the SOA mass. Among the remaining ions that partition between the two phases, only 18 are considered in Fig.5a, either because they are important in terms of mass or because they are considered parent ions following Gkatzelis et al. (2018) method. About 24 to 58 % of the particle mass populates the SVOCs regime, while 8 to 16 % are in the IVOCs regime, depending on the experimental conditions. In a recent work the SOA components from OH radical oxidation of toluene populated mostly the SVOC range and only 10-17 % was exclusively in the particle phase (Lannuque et al., 2023), probably because of higher initial VOC concentration and lower OH exposure (10-20 h compared to 1.3-3 days in this study) leading to a less advanced oxidation. But overall, the effect of temperature observed is quite similar for the two chemical systems. For naphthalene at 280 K, out of the 110 ions detected in the particle phase, 40 ions are exclusively observed in the particle phase, making up 5 % only of the condensed mass fraction. For the selected 20 compounds that partition between the two phases, approximately 78-95 % of their SOA mass populates the SVOC regime and 3-17 % lies in the IVOC portion. The larger skeleton structure of naphthalene oxidation products, even first generation, can explain the high fraction of SOA in the SVOC regime (predominantly $C_{8\text{-}10}$ compounds) as confirmed by the O/C range, lower for naphthalene than for m-xylene.

The derived saturation concentration (C_i^*) values range between 1 to 6919 μg m^{-3}, comparable to other SOA systems (Gkatzelis et al., 2018; Kostenidou et al., 2024; Lannuque et al., 2023). Previous studies on biogenic VOCs reported a decreasing volatility with increasing OSc (Gkatzelis et al., 2018; Jimenez et al., 2009; Kroll et al., 2011), while the present works and previous investigations on anthropogenic VOCs (toluene and gasoline vehicle emissions) did not confirm such a trend (Kostenidou et al., 2024; Lannuque et al., 2023).

Figures 5c and 5d present the difference of $\log_{10}C_i^*$ between the two experiments conducted at 280 and 295 K, $\Delta\log_{10}C_i^*$. Its values vary from 0.06 to 1.08 as a function of carbon number and oxygen number (tables S2 and S3). For m-xylene oxidation products (Fig. 5c), $\Delta\log_{10}C_i^*$ decreases with increasing carbon number. Indeed, the C_5-C_8 products bearing 3 to 5 oxygen atoms (darker green markers) lie at the bottom of the plot generally exhibiting $\Delta\log_{10}C_i^*$ values below 0.4, emphasizing the effect of oxygen atoms in reducing the volatility of these compounds. The C_3 compounds, tentatively associated to methylglyoxal and propanoic acid, exhibit also moderate $\Delta\log_{10}C_i^*$, probably because they are still volatile even at the lower experimental temperatures (Table 2). Only few among the identified C_4-C_5 products exhibit $\Delta\log_{10}C_i^*$ values above 0.6 and are tentatively identified as ring opening products, with multiple functional groups increasing their polarity (aldehydes, acids and furandiones).

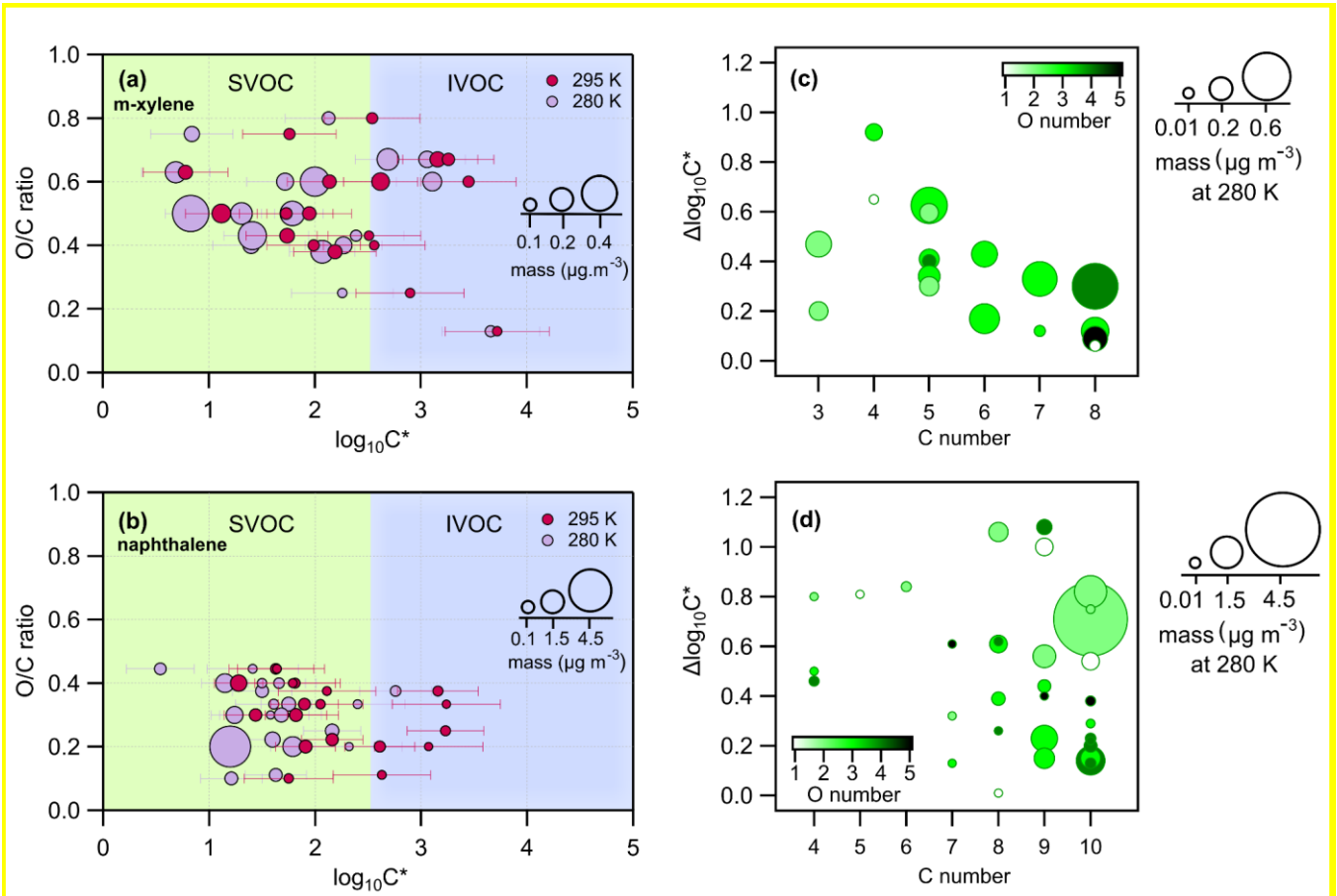

Figure 5. Panels (a) and (b) present the 2D-VBS framework: the O/C ratio (y-axis) for the detected parent ions of m-xylene and naphthalene photooxidation, respectively, as a function of saturation concentration ($\log_{10}C_i^*$ in µg m^{-3}; x-axis) for high NO_x experiments. The size of the circles denotes the mass of each species. Experiments carried out at 280 K are in light violet while the ones carried out at 295 K are in magenta. The light green and the light blue background shadings correspond to the SVOC ($0 < \log_{10}C_i^* < 2.5$) and the IVOC ($2.5 < \log_{10}C_i^* < 5$) regimes, respectively. Panels (c) and (d) present $\Delta\log_{10}C_i^*$ (the difference of $\log_{10}C_i^*$ between experiments at 280 K and 295 K; y-axis) as function of carbon number (x-axis), color scaled by oxygen number and sized by the mass (in µg m^{-3}) of each compound at 280 K for m-xylene and naphthalene oxidation products, respectively.

Naphthalene oxidation products on the other hand (Fig. 5d) have $\Delta\log_{10}C_i^*$ over a similar range compared to m-xylene, but exhibit a different behaviour. Most of the relevant reaction products are associated to $C_{8\text{-}10}H_{4\text{-}10}O_{1\text{-}4}$ products, accounting for 90 % of the SOA mass and have at least one aromatic ring. These compounds belong SVOC with a $\log_{10}C_i^* < 2$, and span a broad range of $\Delta\log_{10}C_i^*$ depending on the number of oxygen atoms (from 1 to 5) and the specific functionalities. Logically, the most oxygenated C_{10} are poorly affected by temperature, since they are the least volatile and already mostly in the particle phase at 295 K. Compared to m-xylene, the most important naphthalene SOA-products are less oxygenated and seem to be more temperature-sensitive.

3.4 Comparison of experimentally derived and calculated volatilities

The experimentally derived volatilities are here compared to the estimated ones from pure-liquid saturation vapour pressure using Volcalc based on SIMPOL.1 (Meredith et al., 2023; Pankow and Asher, 2008; Riemer, 2023). Volatilities from the two methods are presented in Figs. 6a and 6b for both m-xylene and naphthalene oxidation products at 280 K, respectively. A considerable discrepancy is observed between the experimental and calculated values, the latter ones spanning a larger range of volatilities. For m-xylene SOA, the theoretical approach tends to largely overestimate the volatility of small and oxygenated compounds below *m*/*z* 120, similarly to recent investigations using different techniques as SV-TAG coupled to GC-MS, thermal desorption-AMS and FIGAERO-CIMS and CHARON (Stark et al., 2017; Ijaz et al., 2024; Liang et al., 2023).

For some light carbonyl compounds present among the m-xylene reaction products, the disagreement can be potentially explained by presence of ammonium ions (NH_4^+) in the seeds that can act as a catalyst for accretion reactions such as aldol condensation (Li et al., 2022, 2011; Nozière et al., 2010; Sareen et al., 2010) as well as acetal and hemiacetal formation (Jang et al., 2002; Li et al., 2022; Loeffler et al., 2006; Shapiro et al., 2009) shifting the equilibrium to the condensed phase for these molecules. Furthermore, Lannuque et al. (2023) have achieved better model representation of experimental SOA mass concentration after including interactions between aldehydes as methylglyoxal and inorganic compounds (such as ammonium). Those reactions are also catalyzed in the presence of water, especially for highly oxidized hydrophilic compounds (Meng et al., 2024). For some other compounds, as functionalized acids and some dialdehydes, disagreements may arise from the fragmentation in the mass spectrometer. Despite a relatively low *E*/*N* value (68 Td) used in this work, fragmentation may still occur, particularly in polyfunctional products (Leglise et al., 2019). We also tested the fragmentation of several compounds in a separate work (Lannuque et al., 2023) where we could observe low or negligible fragmentation for methylglyoxal, furans, furfurals, maleic acids and anhydrides but important fragmentation for small linear aldehydes.

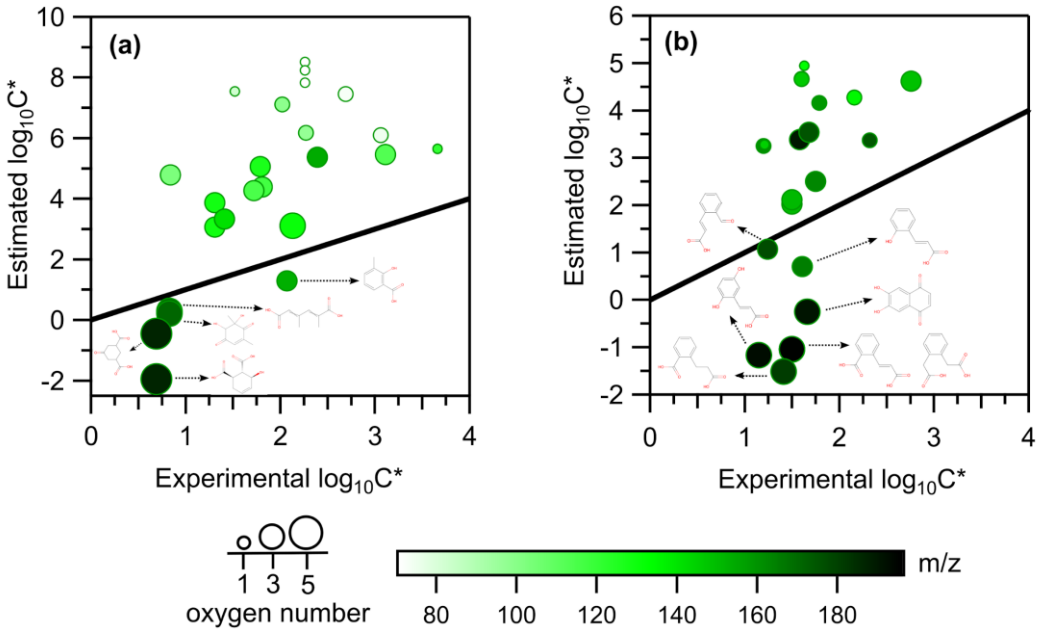

Figure 6. Theoretical (y-axis) versus experimental $\log_{10}C_i^*$ values (x-axis) for (a) m-xylene and (b) naphthalene oxidation products at 280 K under high NO_x conditions. The black line is the 1:1 fit. The size of the markers is proportional to the oxygen number. The color gradient corresponds to *m*/*z* of the detected compounds.

For naphthalene SOA products, larger discrepancies are observed for larger compounds ($m/z \geq 160$) associated to C_{8-10} compounds bearing multiple functional groups. For such types of compounds, the model predicts very low volatilities (O'Meara et al., 2014) also demonstrating that SIMPOL.1 consistently overestimates temperature-induced volatility changes for highly oxygenated compounds (such as hydroxylated ketones and diacids). These discrepancies are attributed to the additive nature of SIMPOL.1's functional group contribution framework. At 280 K, a carboxylic acid group (-COOH) decreases the saturation vapor pressure by nearly a factor of 6000, a hydroxyl group (-OH) by factor 200, while a ketone group (=O) reduces it by less than a factor of 9. It is also worth noting that multiple structural isomers are not distinguished in our work, and this may also introduce some uncertainties. An example is provided by 1,2-naphthoquinone and 1,4-naphthoquinone owing quite different vapor pressure making the former potentially more interesting in the particle phase (McWhinney et al., 2013). Liang et al. (2023) and Dang et al., (2019) also reported very different gas-particle partitioning behavior and vapor pressures values among isomers. Barley and McFiggans (2010) and Peräkylä et al. (2020) highlighted significant overpredictions for diacids and polyfunctional compounds, attributing these errors to the model's parameterizations and group contributions. This work therefore aligns with previous findings and suggests that vapor pressures of multifunctional compounds of the aerosol are still not well estimated by models.

Figure S7 shows the comparison of estimated versus experimental $\log_{10}C_i^*$ values at 295 K under high NO_x conditions for both m-xylene and naphthalene. These results closely match those at 280 K (Fig. 6), with no significant difference in the distribution.

Figure S8 presents the same analysis under low NO_x conditions at 295 K, which similarly shows no notable deviation from the trends observed at low NO_x (Fig. S7). This indicates that neither temperature nor NO_x regime substantially explain the model-observation discrepancy in our dataset. Temperature-induced volatility changes are quantified in Figs. 5c,d which represents the difference between experimental $\log_{10}C_i^*$ at 280 K and 295 K (i.e. $\Delta\log_{10}C_i^*$) against the C number. The temperature effect on the discrepancy between the experimental and the estimated $\log_{10}C_i^*$ values is presented in Fig. S9. The values of $\Delta\log_{10}C_i^*$, the difference between estimated and experimental $\log_{10}C_i^*$, for the oxidation products of m-xylene (Fig. S9a) and naphthalene (Fig. S9b) is plotted as a function *m*/*z*, at 295 K and 280 K. The discrepancies at both temperatures are quite close to each other. Overall, SIMPOL.1's bias in predicting volatility for oxidation products is not strongly affected by temperature. This consistent discrepancy with temperature and NO_x confirmed that partitioning of organic compounds is more complex than the simple evaporation of compounds isolated, and that surface interactions and bulk chemical reactions are potential important drivers affecting partitioning equilibria.

4 Conclusion

This study presents a detailed experimental investigation of the OH-initiated photooxidation of two anthropogenic aromatic precursors, m-xylene and naphthalene, using an OFR under different NO_x and temperature conditions. For both precursors, SOA yields are found to strongly increase when temperature and NO_x decrease, in agreement with previous studies. The CHARON-inlet coupled to a PTR-ToF-MS successfully quantified between 65-80 % of the total organic mass covered by an aerosol mass spectrometer (HR-ToF-AMS). Major products both in the gas and particulate phases are confirmed based PTR-ToF-MS inferred molecular formula and intercomparison with the literature. Major gas phase products of m-xylene SOA are C_3, C_5 and C_8 compounds whereas the particle phase products are dominated by C_6-C_8 compounds. This pattern is consistent through different temperatures, indicating similar chemistry in these conditions. For naphthalene experiments, gas phase products are dominated by C_8 and C_{10} compounds, while the particle phase composition mainly consists of C_8, C_9 and C_{10} compounds. Nitro-derivatives (nitrogen containing compounds + PAN fragment) measured in both phases did not exceed 7 % in naphthalene experiments whereas they could reach up to 20 % in the m-xylene experiments. The similarity in product distributions under both high and low NO_x conditions for both m-xylene and naphthalene indicates that the chemical reactions were largely unaffected by the NO_x levels, implying that NO_x had minimal influence on oxidant concentrations in the OFR.

The volatility properties of the individual compounds are presented in the 2D-VBS framework: 24-58 % of the SOA mass generated by m-xylene populates the SVOC regime and 8-16 % populates the IVOCs regime, while the naphthalene SOA mass is mostly (up to 95 %) found in the SVOC regime. No clear correlation could be observed between the volatility values and the increasing oxidation state (OSc), in agreement with previous studies on anthropogenic monoaromatic precursors. Temperature variation, from 295 to 280 K, induced an expected decrease in volatility ($\Delta\log_{10}C_i^*$), this decrease ranging from 0.06 to 1.08. The magnitude of $\Delta\log_{10}C_i^*$ seems to be controlled by multiple parameters, as temperature, carbon number, oxygen number and specific chemical moieties. When experimentally derived volatilities are compared to a group contribution

parameterization model based on pure liquid vapor pressure (SIMPOL.1), large discrepancies are observed. The small discrepancies between estimated and experimental $\log_{10}C_i^*$ at both temperatures indicate that the temperature has little impact on SIMPOL.1's bias in predicting the volatility of oxidation products. The difference between estimated and experimental volatilities highlight the complexity of gas-particle partitioning, and the limit of parameterizations that should be further validated using larger datasets from various measurement techniques and experimental conditions.

This study advances our understanding of SOA composition and gas-particle partitioning at different and relevant atmospheric conditions and also holds some implications for urban air quality management and climate modelling. The observed temperature-dependent shifts in SOA mass loadings and volatility highlight the importance of accounting for seasonal variations, particularly in urban areas with high anthropogenic VOC emissions. Furthermore, the findings underscore the need to refine current air quality and climate models by incorporating more recent findings and real-world atmospheric conditions, paving the way for more accurate predictions of aerosol impacts on air quality, climate, and public health.

Data availability

Finalized data are mostly available in supplementary material. More detailed data are available on request.

Supplementary material

Competing interests

The authors declare that they have no conflict of interest.

Author contribution

MS, JK, and BD designed the experimental setup. MS, JK, BTR and BD performed the experiments and data treatment. MS, BD and JK analysed and interpreted the data. MS ran the SIMPOL.1 model. MS drafted the article. All the co-authors revised the article.

Financial Support

This work was funded by the POLEMICS project of the Agence Nationale de la Recherche (ANR) program (grant ANR-18-CE22-0011), and the MAESTRO-EU6 project (ADEME CORTEA n. 1866C0001), the French government under the France 2030 investment plan, as part of the Initiative d'Excellence d'Aix-Marseille Université – A*MIDEX " AMX-21-PEP-016, the French national research agency (ANR-22-CE22-0003-01) and the Environmental Sciences doctoral school (ED 251). BD

acknowledges the MITI program from CNRS for the financial support allowing the design and the construction of the new oxidation flow reactor (OFR) deployed in this study.

References

Ahlberg, E., Eriksson, A., Brune, W. H., Roldin, P., and Svenningsson, B.: Effect of salt seed particle surface area, composition and phase on secondary organic aerosol mass yields in oxidation flow reactors, Atmos. Chem. Phys., 19, 2701–2712, https://doi.org/10.5194/acp-19-2701-2019, 2019.

Ahn, J., Rao, G., and Vejerano, E.: Temperature dependence of the gas-particle partitioning of selected VOCs, Environ. Sci.: Processes Impacts, 23, 947–955, https://doi.org/10.1039/D1EM00176K, 2021.

Anderson, J. O., Thundiyil, J. G., and Stolbach, A.: Clearing the Air: A Review of the Effects of Particulate Matter Air Pollution on Human Health, J. Med. Toxicol., 8, 166–175, https://doi.org/10.1007/s13181-011-0203-1, 2012.

Aoki, N., Inomata, S., and Tanimoto, H.: Detection of C1–C5 alkyl nitrates by proton transfer reaction time-of-flight mass spectrometry, International Journal of Mass Spectrometry, 263, 12–21, https://doi.org/10.1016/j.ijms.2006.11.018, 2007.

Atkinson, R., Aschmann, S. M., and Zielinska, B.: GAS-PHASE ATMOSPHERIC CHEMISTRY OF l- AND 2-NITRONAPHTHALENE AND 1,4-NAPHTHOQUINONE, 1989.

Atkinson, R., Aschmann, S. M., and Arey, J.: Formation of ring-retaining products from the OH radical-initated reactions of *o* -, *m* -, and *p* -xylene, Int J of Chemical Kinetics, 23, 77–97, https://doi.org/10.1002/kin.550230108, 1991.

Aumont, B., Camredon, M., Mouchel-Vallon, C., La, S., Ouzebidour, F., Valorso, R., Lee-Taylor, J., and Madronich, S.: Modeling the influence of alkane molecular structure on secondary organic aerosol formation, Faraday Discuss., 165, 105, https://doi.org/10.1039/c3fd00029j, 2013.

Bahrami, A., Haghighat, F., and Zhu, J.: Indoor environment gas-particle partitioning models of SVOCs and impact of particle properties on the partitioning: A review., Building & Environment, 262, N.PAG, https://doi.org/10.1016/j.buildenv.2024.111791, 2024.

Barley, M. H. and McFiggans, G.: The critical assessment of vapour pressure estimation methods for use in modelling the formation of atmospheric organic aerosol, Atmos. Chem. Phys., 10, 749–767, https://doi.org/10.5194/acp-10-749-2010, 2010.

Baudic, A., Gros, V., Sauvage, S., Locoge, N., Sanchez, O., Sarda-Estève, R., Kalogridis, C., Petit, J.-E., Bonnaire, N., Baisnée, D., Favez, O., Albinet, A., Sciare, J., and Bonsang, B.: Seasonal variability and source apportionment of volatile organic compounds (VOCs) in the Paris megacity (France), Atmos. Chem. Phys., 16, 11961–11989, https://doi.org/10.5194/acp-16-11961-2016, 2016.

Berlinger, B., Fehérvári, P., Kővágó, C., Lányi, K., Mátis, G., Mackei, M., and Könyves, L.: There Is Still a Need for a Comprehensive Investigation of the Health Consequences of Exposure to Urban Air with Special Regard to Particulate Matter (PM) and Cardiovascular Effects, Atmosphere, 15, 296, https://doi.org/10.3390/atmos15030296, 2024.

Birdsall, A. W. and Elrod, M. J.: Comprehensive NO-Dependent Study of the Products of the Oxidation of Atmospherically Relevant Aromatic Compounds, J. Phys. Chem. A, 115, 5397–5407, https://doi.org/10.1021/jp2010327, 2011.

Bloss, C., Wagner, V., Jenkin, M. E., Volkamer, R., Bloss, W. J., Lee, J. D., Heard, D. E., Wirtz, K., Martin-Reviejo, M., Rea, G., Wenger, J. C., and Pilling, M. J.: Development of a detailed chemical mechanism (MCMv3.1) for the atmospheric oxidation of aromatic hydrocarbons, Atmos. Chem. Phys., 5, 641–664, https://doi.org/10.5194/acp-5-641-2005, 2005.

Bosque, R. and Sales, J.: Polarizabilities of Solvents from the Chemical Composition, J. Chem. Inf. Comput. Sci., 42, 1154–1163, https://doi.org/10.1021/ci025528x, 2002.

Bunce, N. J., Liu, L., Zhu, J., and Lane, D. A.: Reaction of Naphthalene and Its Derivatives with Hydroxyl Radicals in the Gas Phase, Environ. Sci. Technol., 31, 2252–2259, https://doi.org/10.1021/es960813g, 1997.

Calvert, J. G., Atkinson, R., Becker, K. H., Kamens, R. M., Wallington, T. H., Seinfeld, J. H., and Yarwood, G.: The Mechanisms of Atmospheric Oxidation of Aromatic Hydrocarbons, Oxford University Press, 2002.

Calvert, J. G., Orlando, J. J., Stockwell, W. R., and Wallington, T. J.: The Mechanisms of Reactions Influencing Atmospheric Ozone, Oxford University Press, https://doi.org/10.1093/oso/9780190233020.001.0001, 2015.

Canagaratna, M. R., Jayne, J. T., Jimenez, J. L., Allan, J. D., Alfarra, M. R., Zhang, Q., Onasch, T. B., Drewnick, F., Coe, H., Middlebrook, A., Delia, A., Williams, L. R., Trimborn, A. M., Northway, M. J., DeCarlo, P. F., Kolb, C. E., Davidovits, P., and Worsnop, D. R.: Chemical and microphysical characterization of ambient aerosols with the aerodyne aerosol mass spectrometer, Mass Spectrometry Reviews, 26, 185–222, https://doi.org/10.1002/mas.20115, 2007.

Cappa, C. D. and Wilson, K. R.: Multi-generation gas-phase oxidation, equilibrium partitioning, and the formation and evolution of secondary organic aerosol, Atmos. Chem. Phys., 12, 9505–9528, https://doi.org/10.5194/acp-12-9505-2012, 2012.

Chan, A. W. H., Kautzman, K. E., Chhabra, P. S., Surratt, J. D., Chan, M. N., Crounse, J. D., Wennberg, P. O., Flagan, R. C., and Seinfeld, J. H.: Secondary organic aerosol formation from photooxidation of naphthalene and alkylnaphthalenes: implications for oxidation of intermediate volatility organic compounds (IVOCs), Atmos. Chem. Phys., 9, 3049–3060, https://doi.org/10.5194/acp-9-3049-2009, 2009.

Chen, C.-L., Kacarab, M., Tang, P., and Cocker, D. R.: SOA formation from naphthalene, 1-methylnaphthalene, and 2-methylnaphthalene photooxidation, Atmospheric Environment, 131, 424–433, https://doi.org/10.1016/j.atmosenv.2016.02.007, 2016.

Chen, C.-L., Li, L., Tang, P., and Cocker, D. R.: SOA formation from photooxidation of naphthalene and methylnaphthalenes with m-xylene and surrogate mixtures, Atmospheric Environment, 180, 256–264, https://doi.org/10.1016/j.atmosenv.2018.02.051, 2018.

Chen, T., Chu, B., Ma, Q., Zhang, P., Liu, J., and He, H.: Effect of relative humidity on SOA formation from aromatic hydrocarbons: Implications from the evolution of gas- and particle-phase species, Science of The Total Environment, 773, 145015, https://doi.org/10.1016/j.scitotenv.2021.145015, 2021.

Chen, T., Liu, Y., Chu, B., Liu, C., Liu, J., Ge, Y., Ma, Q., Ma, J., and He, H.: Differences of the oxidation process and secondary organic aerosol formation at low and high precursor concentrations, Journal of Environmental Sciences, 79, 256–263, https://doi.org/10.1016/j.jes.2018.11.011, 2019.

Clark, C. H., Kacarab, M., Nakao, S., Asa-Awuku, A., Sato, K., and Cocker, D. R.: Temperature Effects on Secondary Organic Aerosol (SOA) from the Dark Ozonolysis and Photo-Oxidation of Isoprene, Environ. Sci. Technol., 50, 5564–5571, https://doi.org/10.1021/acs.est.5b05524, 2016.

Dang, C., Bannan, T., Shelley, P., Priestley, M., Worrall, S. D., Waters, J., Coe, H., Percival, C. J., and Topping, D.: The effect of structure and isomerism on the vapor pressures of organic molecules and its potential atmospheric relevance, Aerosol Science and Technology, 53, 1040–1055, https://doi.org/10.1080/02786826.2019.1628177, 2019.

DeCarlo, P. F., Kimmel, J. R., Trimborn, A., Northway, M. J., Jayne, J. T., Aiken, A. C., Gonin, M., Fuhrer, K., Horvath, T., Docherty, K. S., Worsnop, D. R., and Jimenez, J. L.: Field-Deployable, High-Resolution, Time-of-Flight Aerosol Mass Spectrometer, Analytical Chemistry, 78, 8281–8289, https://doi.org/10.1021/ac061249n, 2006.

Deng, Y., Inomata, S., Sato, K., Ramasamy, S., Morino, Y., Enami, S., and Tanimoto, H.: Temperature and acidity dependence of secondary organic aerosol formation from α -pinene ozonolysis with a compact chamber system, Atmos. Chem. Phys., 21, 5983–6003, https://doi.org/10.5194/acp-21-5983-2021, 2021.

Dodge, M.: Combined use of modeling techniques and smog chamber data to derive ozone-precursor relationships, International conference on photochemical oxidant pollution and its control: Proceedings, 881–889, 1977.

Donahue, N. M., Robinson, A. L., Stanier, C. O., and Pandis, S. N.: Coupled Partitioning, Dilution, and Chemical Aging of Semivolatile Organics, Environ. Sci. Technol., 40, 2635–2643, https://doi.org/10.1021/es052297c, 2006.

Donahue, N. M., Epstein, S. A., Pandis, S. N., and Robinson, A. L.: A two-dimensional volatility basis set: 1. organic-aerosol mixing thermodynamics, Atmos. Chem. Phys., 11, 3303–3318, https://doi.org/10.5194/acp-11-3303-2011, 2011.

Donahue, N. M., Kroll, J. H., Pandis, S. N., and Robinson, A. L.: A two-dimensional volatility basis set – Part 2: Diagnostics of organic-aerosol evolution, Atmos. Chem. Phys., 12, 615–634, https://doi.org/10.5194/acp-12-615-2012, 2012.

Duncianu, M., David, M., Kartigueyane, S., Cirtog, M., Doussin, J.-F., and Picquet-Varrault, B.: Measurement of alkyl and multifunctional organic nitrates by proton-transfer-reaction mass spectrometry, Atmos. Meas. Tech., 10, 1445–1463, https://doi.org/10.5194/amt-10-1445-2017, 2017.

Eichler, P., Müller, M., D'Anna, B., and Wisthaler, A.: A novel inlet system for online chemical analysis of semi-volatile submicron particulate matter, Atmos. Meas. Tech., 8, 1353–1360, https://doi.org/10.5194/amt-8-1353-2015, 2015.

European Environment Agency: Europe's air quality status 2021, Publications Office, LU, 2022.

Fan, J. and Zhang, R.: Density Functional Theory Study on OH-Initiated Atmospheric Oxidation of *m* -Xylene, J. Phys. Chem. A, 112, 4314–4323, https://doi.org/10.1021/jp077648j, 2008.

Fan, C., Wang, W., Wang, K., Lei, T., Xiang, W., Hou, C., Li, J., Guo, Y., and Ge, M.: Temperature effects on SOA formation of n-dodecane reaction initiated by Cl atoms, Atmospheric Environment, 346, 121070, https://doi.org/10.1016/j.atmosenv.2025.121070, 2025.

Fang, H., Luo, S., Huang, X., Fu, X., Xiao, S., Zeng, J., Wang, J., Zhang, Y., and Wang, X.: Ambient naphthalene and methylnaphthalenes observed at an urban site in the Pearl River Delta region: Sources and contributions to secondary organic aerosol, Atmospheric Environment, 252, 118295, https://doi.org/10.1016/j.atmosenv.2021.118295, 2021.

Fang, H., Wang, W., Xu, H., Huang, Y., Jiang, H., Wu, T., Li, J., Zha, S., Zhang, J., Zhou, R., and Wang, X.: Sources and secondary transformation potentials of aromatic hydrocarbons observed in a medium-sized city in yangtze river delta region: Emphasis on intermediate-volatility naphthalene, Atmospheric Environment, 318, 120239, https://doi.org/10.1016/j.atmosenv.2023.120239, 2024.

Forstner, H. J. L., Flagan, R. C., and Seinfeld, J. H.: Secondary Organic Aerosol from the Photooxidation of Aromatic Hydrocarbons: Molecular Composition, Environ. Sci. Technol., 31, 1345–1358, https://doi.org/10.1021/es9605376, 1997.

Gioumousis, G. and Stevenson, D. P.: Reactions of Gaseous Molecule Ions with Gaseous Molecules. V. Theory, The Journal of Chemical Physics, 29, 294–299, https://doi.org/10.1063/1.1744477, 1958.

Gkatzelis, G. I., Hohaus, T., Tillmann, R., Gensch, I., Müller, M., Eichler, P., Xu, K.-M., Schlag, P., Schmitt, S. H., Yu, Z., Wegener, R., Kaminski, M., Holzinger, R., Wisthaler, A., and Kiendler-Scharr, A.: Gas-to-particle partitioning of major biogenic oxidation products: a study on freshly formed and aged biogenic SOA, Atmos. Chem. Phys., 18, 12969–12989, https://doi.org/10.5194/acp-18-12969-2018, 2018.

Heald, C. L., Jacob, D. J., Park, R. J., Russell, L. M., Huebert, B. J., Seinfeld, J. H., Liao, H., and Weber, R. J.: A large organic aerosol source in the free troposphere missing from current models, Geophysical Research Letters, 32, 2005GL023831, https://doi.org/10.1029/2005GL023831, 2005.

Healy, R. M., Chen, Y., Kourtchev, I., Kalberer, M., O'Shea, D., and Wenger, J. C.: Rapid Formation of Secondary Organic Aerosol from the Photolysis of 1-Nitronaphthalene: Role of Naphthoxy Radical Self-reaction, Environ. Sci. Technol., 46, 11813–11820, https://doi.org/10.1021/es302841j, 2012.

Henze, D. K., Seinfeld, J. H., Ng, N. L., and Kroll, J. H.: Global modeling of secondary organic aerosol formation from aromatic hydrocarbons: high- vs. low-yield pathways, Atmos. Chem. Phys., 8, 2405–2421, https://doi.org/10.5194/acp-8-2405-2008, 2008.

Huang, D. D., Kong, L., Gao, J., Lou, S., Qiao, L., Zhou, M., Ma, Y., Zhu, S., Wang, H., Chen, S., Zeng, L., and Huang, C.: Insights into the formation and properties of secondary organic aerosol at a background site in Yangtze River Delta region of China: Aqueous-phase processing vs. photochemical oxidation, Atmospheric Environment, 239, 117716, https://doi.org/10.1016/j.atmosenv.2020.117716, 2020.

Huang, M., Zhang, W., Hao, L., Wang, Z., Zhao, W., Gu, X., and Fang, L.: Low-Molecular Weight and Oligomeric Components in Secondary Organic Aerosol from the Photooxidation of p-Xylene, J Chinese Chemical Soc, 55, 456–463, https://doi.org/10.1002/jccs.200800068, 2008.

Huang, R.-J., Zhang, Y., Bozzetti, C., Ho, K.-F., Cao, J.-J., Han, Y., Daellenbach, K. R., Slowik, J. G., Platt, S. M., Canonaco, F., Zotter, P., Wolf, R., Pieber, S. M., Bruns, E. A., Crippa, M., Ciarelli, G., Piazzalunga, A., Schwikowski, M., Abbaszade, G., Schnelle-Kreis, J., Zimmermann, R., An, Z., Szidat, S., Baltensperger, U., Haddad, I. E., and Prévôt, A. S. H.: High secondary aerosol contribution to particulate pollution during haze events in China, Nature, 514, 218–222, https://doi.org/10.1038/nature13774, 2014.

Ijaz, A., Temime-Roussel, B., Kammer, J., Mao, J., Simpson, W., Law, K. S., and Barbara, D.: In situ measurements of gas-particle partitioning of organic compounds in Fairbanks, Faraday Discuss., 10.1039.D4FD00175C, https://doi.org/10.1039/D4FD00175C, 2024.

Isaacman-VanWertz, G., Massoli, P., O'Brien, R., Lim, C., Franklin, J. P., Moss, J. A., Hunter, J. F., Nowak, J. B., Canagaratna, M. R., Misztal, P. K., Arata, C., Roscioli, J. R., Herndon, S. T., Onasch, T. B., Lambe, A. T., Jayne, J. T., Su, L., Knopf, D. A., Goldstein, A. H., Worsnop, D. R., and Kroll, J. H.: Chemical evolution of atmospheric organic carbon over multiple generations of oxidation, Nature Chem, 10, 462–468, https://doi.org/10.1038/s41557-018-0002-2, 2018.

Jang, M. and Kamens, R. M.: Characterization of Secondary Aerosol from the Photooxidation of Toluene in the Presence of NO_x and 1-Propene, Environ. Sci. Technol., 35, 3626–3639, https://doi.org/10.1021/es010676+, 2001.

Jang, M., Czoschke, N. M., Lee, S., and Kamens, R. M.: Heterogeneous Atmospheric Aerosol Production by Acid-Catalyzed Particle-Phase Reactions, Science, New Series, 298, 814–817, https://doi.org/10.1126/science.1075798, 2002.

Jenkin, M. E., Saunders, S. M., Wagner, V., and Pilling, M. J.: Protocol for the development of the Master Chemical Mechanism, MCM v3 (Part B): tropospheric degradation of aromatic volatile organic compounds, Part B, 2003.

Jiang, Z., Grosselin, B., Daële, V., Mellouki, A., and Mu, Y.: Seasonal and diurnal variations of BTEX compounds in the semi-urban environment of Orleans, France, Science of The Total Environment, 574, 1659–1664, https://doi.org/10.1016/j.scitotenv.2016.08.214, 2017.

Jimenez, J. L., Canagaratna, M. R., Donahue, N. M., Prevot, A. S. H., Zhang, Q., Kroll, J. H., DeCarlo, P. F., Allan, J. D., Coe, H., Ng, N. L., Aiken, A. C., Docherty, K. S., Ulbrich, I. M., Grieshop, A. P., Robinson, A. L., Duplissy, J., Smith, J. D., Wilson, K. R., Lanz, V. A., Hueglin, C., Sun, Y. L., Tian, J., Laaksonen, A., Raatikainen, T., Rautiainen, J., Vaattovaara, P., Ehn, M., Kulmala, M., Tomlinson, J. M., Collins, D. R., Cubison, M. J., E., Dunlea, J., Huffman, J. A., Onasch, T. B., Alfarra, M. R., Williams, P. I., Bower, K., Kondo, Y., Schneider, J., Drewnick, F., Borrmann, S., Weimer, S., Demerjian, K., Salcedo, D., Cottrell, L., Griffin, R., Takami, A., Miyoshi, T., Hatakeyama, S., Shimono, A., Sun, J. Y., Zhang, Y. M., Dzepina, K., Kimmel, J. R., Sueper, D., Jayne, J. T., Herndon, S. C., Trimborn, A. M., Williams, L. R., Wood, E. C., Middlebrook, A. M., Kolb, C. E., Baltensperger, U., and Worsnop, D. R.: Evolution of Organic Aerosols in the Atmosphere, Science, 326, 1525–1529, https://doi.org/10.1126/science.1180353, 2009.

Jin, Z.-H., Yu, D., Liu, Y.-X., Tian, Z.-Y., Richter, S., Braun-Unkhoff, M., Naumann, C., and Yang, J.-Z.: An experimental investigation of furfural oxidation and the development of a comprehensive combustion model, Combustion and Flame, 226, 200–210, https://doi.org/10.1016/j.combustflame.2020.12.015, 2021.

John, E., Coburn, S., Liu, C., McAughey, J., Mariner, D., McAdam, K. G., Sebestyén, Z., Bakos, I., and Dóbé, S.: Effect of temperature and humidity on the gas–particle partitioning of nicotine in mainstream cigarette smoke: A diffusion denuder study, Journal of Aerosol Science, 117, 100–117, https://doi.org/10.1016/j.jaerosci.2017.12.015, 2018.

Kamens, R. M., Zhang, H., Chen, E. H., Zhou, Y., Parikh, H. M., Wilson, R. L., Galloway, K. E., and Rosen, E. P.: Secondary organic aerosol formation from toluene in an atmospheric hydrocarbon mixture: Water and particle seed effects, Atmospheric Environment, 45, 2324–2334, https://doi.org/10.1016/j.atmosenv.2010.11.007, 2011.

Kang, E., Root, M. J., Toohey, D. W., and Brune, W. H.: Introducing the concept of Potential Aerosol Mass (PAM), Atmos. Chem. Phys., 2007.

Kautzman, K. E., Surratt, J. D., Chan, M. N., Chan, A. W. H., Hersey, S. P., Chhabra, P. S., Dalleska, N. F., Wennberg, P. O., Flagan, R. C., and Seinfeld, J. H.: Chemical Composition of Gas- and Aerosol-Phase Products from the Photooxidation of Naphthalene, J. Phys. Chem. A, 114, 913–934, https://doi.org/10.1021/jp908530s, 2010.

Kim, D.-Y., Soda, S., Kendo, A., and Oh, J.-H.: Atmospheric Photochemistry in Low-and High-NOx Regimes, Journal of Environmental Science International, 16, 1–8, https://doi.org/10.5322/JES.2007.16.1.001, 2007.

Kleindienst, T. E., Jaoui, M., Lewandowski, M., Offenberg, J. H., and Docherty, K. S.: The formation of SOA and chemical tracer compounds from the photooxidation of naphthalene and its methyl analogs in the presence and absence of nitrogen oxides, Atmos. Chem. Phys., 12, 8711–8726, https://doi.org/10.5194/acp-12-8711-2012, 2012.

Klodt, A. L., Aiona, P. K., MacMillan, A. C., Ji (Julie) Lee, H., Zhang, X., Helgestad, T., Novak, G. A., Lin, P., Laskin, J., Laskin, A., Bertram, T. H., Cappa, C. D., and Nizkorodov, S. A.: Effect of relative humidity, NO_x, and ammonia on the physical properties of naphthalene secondary organic aerosols, Environ. Sci.: Atmos., 3, 991–1007, https://doi.org/10.1039/D3EA00033H, 2023.

Kostenidou, E., Marques, B., Temime-Roussel, B., Liu, Y., Vansevenant, B., Sartelet, K., and D'Anna, B.: Secondary organic aerosol formed by Euro 5 gasoline vehicle emissions: chemical composition and gas-to-particle phase partitioning, Atmos. Chem. Phys., 24, 2705–2729, https://doi.org/10.5194/acp-24-2705-2024, 2024.

Kroll, J. H. and Seinfeld, J. H.: Chemistry of secondary organic aerosol: Formation and evolution of low-volatility organics in the atmosphere, Atmospheric Environment, 42, 3593–3624, https://doi.org/10.1016/j.atmosenv.2008.01.003, 2008.

Kroll, J. H., Donahue, N. M., Jimenez, J. L., Kessler, S. H., Canagaratna, M. R., Wilson, K. R., Altieri, K. E., Mazzoleni, L. R., Wozniak, A. S., Bluhm, H., Mysak, E. R., Smith, J. D., Kolb, C. E., and Worsnop, D. R.: Carbon oxidation state as a metric for describing the chemistry of atmospheric organic aerosol, Nature Chem, 3, 133–139, https://doi.org/10.1038/nchem.948, 2011.

La, Y. S., Camredon, M., Ziemann, P. J., Valorso, R., Matsunaga, A., Lannuque, V., Lee-Taylor, J., Hodzic, A., Madronich, S., and Aumont, B.: Impact of chamber wall loss of gaseous organic compounds on secondary organic aerosol formation: explicit modeling of SOA formation from alkane and alkene oxidation, Atmos. Chem. Phys., 16, 1417–1431, https://doi.org/10.5194/acp-16-1417-2016, 2016.

Lambe, A. T., Chhabra, P. S., Onasch, T. B., Brune, W. H., Hunter, J. F., Kroll, J. H., Cummings, M. J., Brogan, J. F., Parmar, Y., Worsnop, D. R., Kolb, C. E., and Davidovits, P.: Effect of oxidant concentration, exposure time, and seed particles on secondary organic aerosol chemical composition and yield, Atmos. Chem. Phys., 15, 3063–3075, https://doi.org/10.5194/acp-15-3063-2015, 2015.

Lamkaddam, H., Gratien, A., Pangui, E., Cazaunau, M., Picquet-Varrault, B., and Doussin, J.-F.: High-NO_x Photooxidation of *n* -Dodecane: Temperature Dependence of SOA Formation, Environ. Sci. Technol., 51, 192–201, https://doi.org/10.1021/acs.est.6b03821, 2017.

Langevin, P. (1872–1946): Une formule fondamentale de théorie cinétique, Ann. Chim. et Physique, 1905, 5, 245, 269–300, 1950.

Languille, B., Gros, V., Petit, J.-E., Honoré, C., Baudic, A., Perrussel, O., Foret, G., Michoud, V., Truong, F., Bonnaire, N., Sarda-Estève, R., Delmotte, M., Feron, A., Maisonneuve, F., Gaimoz, C., Formenti, P., Kotthaus, S., Haeffelin, M., and Favez, O.: Wood burning: A major source of Volatile Organic Compounds during wintertime in the Paris region, Science of The Total Environment, 711, 135055, https://doi.org/10.1016/j.scitotenv.2019.135055, 2020.

Lannuque, V. and Sartelet, K.: Development of a detailed gaseous oxidation scheme of naphthalene for secondary organic aerosol (SOA) formation and speciation, Atmospheric Chemistry and Physics, 24, 8589–8606, https://doi.org/10.5194/acp-24-8589-2024, 2024.

Lannuque, V., Camredon, M., Couvidat, F., Hodzic, A., Valorso, R., Madronich, S., Bessagnet, B., and Aumont, B.: Exploration of the influence of environmental conditions on secondary organic aerosol formation and organic species properties using explicit simulations: development of the VBS-GECKO parameterization, Atmos. Chem. Phys., 18, 13411–13428, https://doi.org/10.5194/acp-18-13411-2018, 2018.

Lannuque, V., D'Anna, B., Kostenidou, E., Couvidat, F., Martinez-Valiente, A., Eichler, P., Wisthaler, A., Müller, M., Temime-Roussel, B., Valorso, R., and Sartelet, K.: Gas–particle partitioning of toluene oxidation products: an experimental and modeling study, Atmos. Chem. Phys., 23, 15537–15560, https://doi.org/10.5194/acp-23-15537-2023, 2023.

Lee, J. Y. and Lane, D. A.: Unique products from the reaction of naphthalene with the hydroxyl radical, Atmospheric Environment, 43, 4886–4893, https://doi.org/10.1016/j.atmosenv.2009.07.018, 2009.

Leglise, J., Müller, M., Piel, F., Otto, T., and Wisthaler, A.: Bulk Organic Aerosol Analysis by Proton-Transfer-Reaction Mass Spectrometry: An Improved Methodology for the Determination of Total Organic Mass, O:C and H:C Elemental Ratios, and the Average Molecular Formula, Anal. Chem., 91, 12619–12624, https://doi.org/10.1021/acs.analchem.9b02949, 2019.

Li, J., Wang, W., Li, K., Zhang, W., Peng, C., Zhou, L., Shi, B., Chen, Y., Liu, M., Li, H., and Ge, M.: Temperature effects on optical properties and chemical composition of secondary organic aerosol derived from *n* -dodecane, Atmos. Chem. Phys., 20, 8123–8137, https://doi.org/10.5194/acp-20-8123-2020, 2020.

Li, K., Wang, W., Ge, M., Li, J., and Wang, D.: Optical properties of secondary organic aerosols generated by photooxidation of aromatic hydrocarbons, Scientific Reports, 4, 4922, https://doi.org/10.1038/srep04922, 2014.

Li, K., Li, J., Liggio, J., Wang, W., Ge, M., Liu, Q., Guo, Y., Tong, S., Li, J., Peng, C., Jing, B., Wang, D., and Fu, P.: Enhanced Light Scattering of Secondary Organic Aerosols by Multiphase Reactions, Environ. Sci. Technol., 51, 1285–1292, https://doi.org/10.1021/acs.est.6b03229, 2017.

Li, K., Li, J., Wang, W., Li, J., Peng, C., Wang, D., and Ge, M.: Effects of Gas-Particle Partitioning on Refractive Index and Chemical Composition of *m* -Xylene Secondary Organic Aerosol, J. Phys. Chem. A, 122, 3250–3260, https://doi.org/10.1021/acs.jpca.7b12792, 2018.

Li, L., Thomsen, D., Wu, C., Priestley, M., Iversen, E. M., Tygesen Skonager, J., Luo, Y., Ehn, M., Roldin, P., Pedersen, H. B., Bilde, M., Glasius, M., and Hallquist, M.: Gas-to-Particle Partitioning of Products from Ozonolysis of Δ^3 -Carene and the Effect of Temperature and Relative Humidity, J. Phys. Chem. A, 128, 918–928, https://doi.org/10.1021/acs.jpca.3c07316, 2024.

Li, Y., Zhao, J., Gomez-Hernandez, M., Lavallee, M., Johnson, N. M., and Zhang, R.: Functionality-based formation of secondary organic aerosol from *m* -xylene photooxidation, Atmos. Chem. Phys., 22, 9843–9857, https://doi.org/10.5194/acp-22-9843-2022, 2022.

Li, Z., Schwier, A. N., Sareen, N., and McNeill, V. F.: Reactive processing of formaldehyde and acetaldehyde in aqueous aerosol mimics: surface tension depression and secondary organic products, Atmos. Chem. Phys., 11, 11617–11629, https://doi.org/10.5194/acp-11-11617-2011, 2011.

Li, Z., Tikkanen, O.-P., Buchholz, A., Hao, L., Kari, E., Yli-Juuti, T., and Virtanen, A.: Effect of Decreased Temperature on the Evaporation of α-Pinene Secondary Organic Aerosol Particles, ACS Earth Space Chem., 3, 2775–2785, https://doi.org/10.1021/acsearthspacechem.9b00240, 2019.

Liang, Y., Wernis, R. A., Kristensen, K., Kreisberg, N. M., Croteau, P. L., Herndon, S. C., Chan, A. W. H., Ng, N. L., and Goldstein, A. H.: Gas–particle partitioning of semivolatile organic compounds when wildfire smoke comes to town, Atmos. Chem. Phys., 23, 12441–12454, https://doi.org/10.5194/acp-23-12441-2023, 2023.

Liu, J., Zhu, S., Guo, T., Jia, B., Xu, L., Chen, J., and Cheng, P.: Smog chamber study of secondary organic aerosol formation from gas- and particle-phase naphthalene ozonolysis, Atmospheric Environment, 294, 119490, https://doi.org/10.1016/j.atmosenv.2022.119490, 2023.

Liu, K., Hua, S., and Song, L.: PM2.5 Exposure and Asthma Development: The Key Role of Oxidative Stress, Oxidative Medicine and Cellular Longevity, 2022, 1–12, https://doi.org/10.1155/2022/3618806, 2022a.

Liu, M. and Matsui, H.: Impacts of Climate Change on Particulate Matter (PM), in: Handbook of Air Quality and Climate Change, edited by: Akimoto, H. and Tanimoto, H., Springer Nature Singapore, Singapore, 1–18, https://doi.org/10.1007/978-981-15-2527-8_39-1, 2020.

Liu, M., Bi, J., and Ma, Z.: Visibility-Based PM $_{2.5}$ Concentrations in China: 1957–1964 and 1973–2014, Environ. Sci. Technol., 51, 13161–13169, https://doi.org/10.1021/acs.est.7b03468, 2017.

Liu, Q., Huang, D. D., Lambe, A. T., Lou, S., Zeng, L., Wu, Y., Huang, C., Tao, S., Cheng, X., Chen, Q., Hoi, K. I., Wang, H., Mok, K. M., Huang, C., and Li, Y. J.: A Comprehensive Characterization of Empirical Parameterizations for OH Exposure in the Aerodyne Potential Aerosol Mass Oxidation Flow Reactor (PAM-OFR), https://doi.org/10.5194/egusphere-2024-2721, 30 September 2024.

Liu, S., Wang, Y., Xu, X., and Wang, G.: Effects of NO2 and RH on secondary organic aerosol formation and light absorption from OH oxidation of o-xylene, Chemosphere, 308, 136541, https://doi.org/10.1016/j.chemosphere.2022.136541, 2022b.

Liu, X., Day, D. A., Krechmer, J. E., Ziemann, P. J., and Jimenez, J. L.: Determining Activity Coefficients of SOA from Isothermal Evaporation in a Laboratory Chamber, Environ. Sci. Technol. Lett., 8, 212–217, https://doi.org/10.1021/acs.estlett.0c00888, 2021.

Loeffler, K. W., Koehler, C. A., Paul, N. M., and De Haan, D. O.: Oligomer Formation in Evaporating Aqueous Glyoxal and Methyl Glyoxal Solutions, Environ. Sci. Technol., 40, 6318–6323, https://doi.org/10.1021/es060810w, 2006.

Loza, C. L., Chhabra, P. S., Yee, L. D., Craven, J. S., Flagan, R. C., and Seinfeld, J. H.: Chemical aging of <i>m</i>-xylene secondary organic aerosol: laboratory chamber study, Atmos. Chem. Phys., 12, 151–167, https://doi.org/10.5194/acp-12-151-2012, 2012.

Lu, H., Huang, Q., Li, J., Ying, Q., Wang, H., Guo, S., Qin, M., and Hu, J.: Simulation of Regional Secondary Organic Aerosol Formation From Monocyclic Aromatic Hydrocarbons Using a Near-Explicit Chemical Mechanism Constrained by Chamber Experiments, JGR Atmospheres, 129, e2023JD040690, https://doi.org/10.1029/2023JD040690, 2024.

Lu, R., Zhou, P., Ma, F., Zhao, Q., Peng, X., Chen, J., and Xie, H.-B.: Multi-generation oxidation mechanism of M-xylene: Unexpected implications for secondary organic aerosol formation, Atmospheric Environment, 327, 120511, https://doi.org/10.1016/j.atmosenv.2024.120511, 2024.

Mao, J., Ren, X., Brune, W. H., Olson, J. R., Crawford, J. H., Fried, A., Huey, L. G., Cohen, R. C., Heikes, B., Singh, H. B., Blake, D. R., Sachse, G. W., Diskin, G. S., Hall, S. R., and Shetter, R. E.: Airborne measurement of OH reactivity during INTEX-B, Atmos. Chem. Phys., 9, 163–173, https://doi.org/10.5194/acp-9-163-2009, 2009.

McWhinney, R. D., Zhou, S., and Abbatt, J. P. D.: Naphthalene SOA: redox activity and naphthoquinone gas–particle partitioning, Atmos. Chem. Phys., 13, 9731–9744, https://doi.org/10.5194/acp-13-9731-2013, 2013.

Meng, X., Wu, Z., Chen, J., Qiu, Y., Zong, T., Song, M., Lee, J., and Hu, M.: Particle phase state and aerosol liquid water greatly impact secondary aerosol formation: insights into phase transition and its role in haze events, Atmos. Chem. Phys., 24, 2399–2414, https://doi.org/10.5194/acp-24-2399-2024, 2024.

Meredith, L. K., Ledford, S. M., Riemer, K., Geffre, P., Graves, K., Honeker, L. K., LeBauer, D., Tfaily, M. M., and Krechmer, J.: Automating methods for estimating metabolite volatility, Front. Microbiol., 14, 1267234, https://doi.org/10.3389/fmicb.2023.1267234, 2023.

Molina, M. J., Zhang, R., Broekhuizen, K., Lei, W., Navarro, R., and Molina, L. T.: Experimental Study of Intermediates from OH-Initiated Reactions of Toluene, J. Am. Chem. Soc., 121, 10225–10226, https://doi.org/10.1021/ja992461u, 1999.

Montero-Montoya, R., López-Vargas, R., and Arellano-Aguilar, O.: Volatile Organic Compounds in Air: Sources, Distribution, Exposure and Associated Illnesses in Children, Annals of Global Health, 84, 225–238, https://doi.org/10.29024/aogh.910, 2018.

Müller, M., Graus, M., Wisthaler, A., Hansel, A., Metzger, A., Dommen, J., and Baltensperger, U.: Analysis of high mass resolution PTR-TOF mass spectra from 1,3,5-trimethylbenzene (TMB) environmental chamber experiments, Atmos. Chem. Phys., 12, 829–843, https://doi.org/10.5194/acp-12-829-2012, 2012.

Müller, M., Mikoviny, T., Jud, W., D'Anna, B., and Wisthaler, A.: A new software tool for the analysis of high resolution PTR-TOF mass spectra, Chemometrics and Intelligent Laboratory Systems, 127, 158–165, https://doi.org/10.1016/j.chemolab.2013.06.011, 2013.

Müller, M., Eichler, P., D'Anna, B., Tan, W., and Wisthaler, A.: Direct Sampling and Analysis of Atmospheric Particulate Organic Matter by Proton-Transfer-Reaction Mass Spectrometry, Anal. Chem., 89, 10889–10897, https://doi.org/10.1021/acs.analchem.7b02582, 2017.

Muller, M., Eicher, P., D'Anna, B., Tan, W., and Wisthaler, A.: Direct Sampling and Analysis of Atmospheric Particulate Organic Matter by Proton-Transfer-Reaction Mass Spectrometry, Analytical Chemistry, 89, 10889–10897, https://doi.org/10.1021/acs.analchem.7b02582, 2017.

Murphy, B. N., Donahue, N. M., Fountoukis, C., Dall'Osto, M., O'Dowd, C., Kiendler-Scharr, A., and Pandis, S. N.: Functionalization and fragmentation during ambient organic aerosol aging: application of the 2-D volatility basis set to field studies, Atmos. Chem. Phys., 12, 10797–10816, https://doi.org/10.5194/acp-12-10797-2012, 2012.

NARSTO. and Electric Power Research Institute.: An assessment of tropospheric ozone pollution : a North American perspective, EPRI, 2000.

Ng, N. L., Kroll, J. H., Chan, A. W. H., Chhabra, P. S., Flagan, R. C., and Seinfeld, J. H.: Secondary organic aerosol formation from m-xylene, toluene, and benzene, Atmos. Chem. Phys., 7, 3909–3922, https://doi.org/10.5194/acp-7-3909-2007, 2007.

Nie, W., Yan, C., Huang, D., Wang, Z., Liu, Y., Qiao, X., Guo, Y., Tian, L., Zheng, P., Xu, Z., Li, Y., Xu, Z., Qi, X., Sun, P., Wang, J., Zheng, F., Li, X., Yin, R., Dallenbach, K., Bianchi, F., Petäjä, T., Zhang, Y., Wang, M., Schervish, M., Wang, S., Qiao, L., Wang, Q., Zhou, M., Wang, H., Yu, C., Yao, D., Guo, H., Ye, P., Lee, S., Li, Y., Liu, Y., Chi, X., Kerminen, V., Ehn, M., Donahue, N., Wang, T., Huang, C., Kulmala, M., Worsnop, D., Jiang, J., and Ding, A.: Secondary organic aerosol formed by condensing anthropogenic vapours over China's megacities, NATURE GEOSCIENCE, 15, 255-+, https://doi.org/10.1038/s41561-022-00922-5, 2022.

Nishino, N., Arey, J., and Atkinson, R.: Formation and Reactions of 2-Formylcinnamaldehyde in the OH Radical-Initiated Reaction of Naphthalene, Environ. Sci. Technol., 43, 1349–1353, https://doi.org/10.1021/es802477s, 2009.

Nozière, B., Dziedzic, P., and Córdova, A.: Inorganic ammonium salts and carbonate salts are efficient catalysts for aldol condensation in atmospheric aerosols, Phys. Chem. Chem. Phys., 12, 3864, https://doi.org/10.1039/b924443c, 2010.

Odum, J. R., Hoffmann, T., Bowman, F., Collins, D., Flagan, R. C., and Seinfeld, J. H.: Gas/Particle Partitioning and Secondary Organic Aerosol Yields, Environ. Sci. Technol., 30, 2580–2585, https://doi.org/10.1021/es950943+, 1996.

Odum, J. R., Jungkamp, T. P. W., Griffin, R. J., Forstner, H. J. L., Flagan, R. C., and Seinfeld, J. H.: Aromatics, Reformulated Gasoline, and Atmospheric Organic Aerosol Formation, Environ. Sci. Technol., 31, 1890–1897, https://doi.org/10.1021/es960535l, 1997.

O'Meara, S., Booth, A. M., Barley, M. H., Topping, D., and McFiggans, G.: An assessment of vapour pressure estimation methods, Phys. Chem. Chem. Phys., 16, 19453–19469, https://doi.org/10.1039/C4CP00857J, 2014.

Pan, S. and Wang, L.: Atmospheric Oxidation Mechanism of *m* -Xylene Initiated by OH Radical, J. Phys. Chem. A, 118, 10778–10787, https://doi.org/10.1021/jp506815v, 2014.

Pang, X.: Biogenic volatile organic compound analyses by PTR-TOF-MS: Calibration, humidity effect and reduced electric field dependency, Journal of Environmental Sciences, 32, 196–206, https://doi.org/10.1016/j.jes.2015.01.013, 2015.

Pankow, J. F. and Asher, W. E.: SIMPOL.1: a simple group contribution method for predicting vapor pressures and enthalpies of vaporization of multifunctional organic compounds, Atmos. Chem. Phys., 8, 2773–2796, https://doi.org/10.5194/acp-8-2773-2008, 2008.

Peng, Y., Wang, H., Gao, Y., Jing, S., Zhu, S., Huang, D., Hao, P., Lou, S., Cheng, T., Huang, C., and Zhang, X.: Real-time measurement of phase partitioning of organic compounds using a proton-transfer-reaction time-of-flight mass spectrometer coupled to aCHARON inlet, ATMOSPHERIC MEASUREMENT TECHNIQUES, 16, 15–28, https://doi.org/10.5194/amt-16-15-2023, 2023.

Peng, Z. and Jimenez, J. L.: Radical chemistry in oxidation flow reactors for atmospheric chemistry research, Chem. Soc. Rev., 49, 2570–2616, https://doi.org/10.1039/C9CS00766K, 2020.

Peräkylä, O., Riva, M., Heikkinen, L., Quéléver, L., Roldin, P., and Ehn, M.: Experimental investigation into the volatilities of highly oxygenated organic molecules (HOMs), Atmos. Chem. Phys., 20, 649–669, https://doi.org/10.5194/acp-20-649-2020, 2020.

Piel, F., Müller, M., Winkler, K., Skytte af Sätra, J., and Wisthaler, A.: Introducing the extended volatility range proton-transfer-reaction mass spectrometer (EVR PTR-MS), Atmos. Meas. Tech., 14, 1355–1363, https://doi.org/10.5194/amt-14-1355-2021, 2021.

Price, D. J., Kacarab, M., Cocker, D. R., Purvis-Roberts, K. L., and Silva, P. J.: Effects of temperature on the formation of secondary organic aerosol from amine precursors, Aerosol Science and Technology, 50, 1216–1226, https://doi.org/10.1080/02786826.2016.1236182, 2016.

Qi, L., Nakao, S., Tang, P., and Iii, D. R. C.: Temperature effect on physical and chemical properties of secondary organic aerosol from m-xylene photooxidation, Atmos. Chem. Phys., https://doi.org/10.5194/acp-10-3847-2010, 2010.

Qi, X., Zhu, S., Zhu, C., Hu, J., Lou, S., Xu, L., Dong, J., and Cheng, P.: Smog chamber study of the effects of NOx and NH3 on the formation of secondary organic aerosols and optical properties from photo-oxidation of toluene, Science of The Total Environment, 727, 138632, https://doi.org/10.1016/j.scitotenv.2020.138632, 2020.

Qu, X., Zhang, Q., and Wang, W.: Mechanism for OH-initiated photooxidation of naphthalene in the presence of O2 and NOx: A DFT study, Chemical Physics Letters, 429, 77–85, https://doi.org/10.1016/j.cplett.2006.08.036, 2006.

Riemer, K.: volcalc: Calculate Volatility of Chemical Compounds, Zenodo, https://doi.org/10.5281/ZENODO.8015155, 2023.

Riva, M.: Caractérisation d'une nouvelle voie de formation d'aérosols organiques secondaires (AOS) dans l'atmosphère: Rôle des précurseurs polyaromatiques, Université Bordeaux 1, 2013.

Rutter, A. P. and Schauer, J. J.: The effect of temperature on the gas–particle partitioning of reactive mercury in atmospheric aerosols, Atmospheric Environment, 41, 8647–8657, https://doi.org/10.1016/j.atmosenv.2007.07.024, 2007.

Salvador, C. M., Chou, C. C.-K., Cheung, H.-C., Ho, T.-T., Tsai, C.-Y., Tsao, T.-M., Tsai, M.-J., and Su, T.-C.: Measurements of submicron organonitrate particles: Implications for the impacts of NOx pollution in a subtropical forest, Atmospheric Research, 245, 105080, https://doi.org/10.1016/j.atmosres.2020.105080, 2020.

Sareen, N., Schwier, A. N., Shapiro, E. L., Mitroo, D., and McNeill, V. F.: Secondary organic material formed by methylglyoxal in aqueous aerosol mimics, Atmos. Chem. Phys., 10, 997–1016, https://doi.org/10.5194/acp-10-997-2010, 2010.

Sarrafzadeh, M., Wildt, J., Pullinen, I., Springer, M., Kleist, E., Tillmann, R., Schmitt, S. H., Wu, C., Mentel, T. F., Zhao, D., Hastie, D. R., and Kiendler-Scharr, A.: Impact of NO_x and OH on secondary organic aerosol formation from β-pinene photooxidation, Atmos. Chem. Phys., 16, 11237–11248, https://doi.org/10.5194/acp-16-11237-2016, 2016.

Sasaki, J., Aschmann, S. M., Kwok, E. S. C., Atkinson, R., and Arey, J.: Products of the Gas-Phase OH and NO_3 Radical-Initiated Reactions of Naphthalene, Environ. Sci. Technol., 31, 3173–3179, https://doi.org/10.1021/es9701523, 1997.

Sato, K., Hatakeyama, S., and Imamura, T.: Secondary Organic Aerosol Formation during the Photooxidation of Toluene: NO_x Dependence of Chemical Composition, J. Phys. Chem. A, 111, 9796–9808, https://doi.org/10.1021/jp071419f, 2007.

Sato, K., Ikemori, F., Ramasamy, S., Iijima, A., Kumagai, K., Fushimi, A., Fujitani, Y., Chatani, S., Tanabe, K., Takami, A., Tago, H., Saito, Y., Saito, S., Hoshi, J., and Morino, Y.: Formation of secondary organic aerosol tracers from anthropogenic and biogenic volatile organic compounds under varied NOx and oxidant conditions, Atmospheric Environment: X, 14, 100169, https://doi.org/10.1016/j.aeaoa.2022.100169, 2022.

Schwantes, R. H., Charan, S. M., Bates, K. H., Huang, Y., Nguyen, T. B., Mai, H., Kong, W., Flagan, R. C., and Seinfeld, J. H.: Low-volatility compounds contribute significantly to isoprene secondary organic aerosol (SOA) under high-NO_x conditions, Atmos. Chem. Phys., 19, 7255–7278, https://doi.org/10.5194/acp-19-7255-2019, 2019.

Seinfeld, J. H. and Pandis, S. N.: Atmospheric chemistry and physics : from air pollution to climate change, Third edition., John Wiley & Sons, Inc. Hoboken, New Jersey, Hoboken, New Jersey, 2016.

Sekimoto, K., Li, S.-M., Yuan, B., Koss, A., Coggon, M., Warneke, C., and De Gouw, J.: Calculation of the sensitivity of proton-transfer-reaction mass spectrometry (PTR-MS) for organic trace gases using molecular properties, International Journal of Mass Spectrometry, 421, 71–94, https://doi.org/10.1016/j.ijms.2017.04.006, 2017.

Shapiro, E. L., Szprengiel, J., Sareen, N., Jen, C. N., Giordano, M. R., and McNeill, V. F.: Light-absorbing secondary organic material formed by glyoxal in aqueous aerosol mimics, Atmos. Chem. Phys., 9, 2289–2300, https://doi.org/10.5194/acp-9-2289-2009, 2009.

Shi, D., Liu, J., Wang, Y., Xu, L., Guo, T., Jia, B., and Cheng, P.: Secondary organic aerosol formation from cis-3-hexen-1-ol/NOx photo-oxidation: The roles of cis-3-hexen-1-ol concentration, illumination intensity, NOx and NH3, Atmospheric Environment, 278, 119090, https://doi.org/10.1016/j.atmosenv.2022.119090, 2022.

Shrivastava, M., Cappa, C. D., Fan, J., Goldstein, A. H., Guenther, A. B., Jimenez, J. L., Kuang, C., Laskin, A., Martin, S. T., Ng, N. L., Petaja, T., Pierce, J. R., Rasch, P. J., Roldin, P., Seinfeld, J. H., Shilling, J., Smith, J. N., Thornton, J. A., Volkamer, R., Wang, J., Worsnop, D. R., Zaveri, R. A., Zelenyuk, A., and Zhang, Q.: Recent advances in understanding secondary organic aerosol: Implications for global climate forcing, Reviews of Geophysics, 55, 509–559, https://doi.org/10.1002/2016RG000540, 2017.

Singh, K. and Tripathi, D.: Particulate Matter and Human Health, in: Environmental Health, edited by: Otsuki, T., IntechOpen, https://doi.org/10.5772/intechopen.100550, 2021.

Song, C., Na, K., and Cocker, D. R.: Impact of the Hydrocarbon to NO $_x$ Ratio on Secondary Organic Aerosol Formation, Environ. Sci. Technol., 39, 3143–3149, https://doi.org/10.1021/es0493244, 2005.

Song, C., Na, K., Warren, B., Malloy, Q., and Cocker, D. R.: Secondary Organic Aerosol Formation from *m* -Xylene in the Absence of NO $_x$, Environ. Sci. Technol., 41, 7409–7416, https://doi.org/10.1021/es070429r, 2007.

Song, C., He, J., Wu, L., Jin, T., Chen, X., Li, R., Ren, P., Zhang, L., and Mao, H.: Health burden attributable to ambient PM2.5 in China, Environmental Pollution, 223, 575–586, https://doi.org/10.1016/j.envpol.2017.01.060, 2017.

Srivastava, D., Vu, T. V., Tong, S., Shi, Z., and Harrison, R. M.: Formation of secondary organic aerosols from anthropogenic precursors in laboratory studies, npj Clim Atmos Sci, 5, 22, https://doi.org/10.1038/s41612-022-00238-6, 2022.

Srivastava, D., Li, W., Tong, S., Shi, Z., and Harrison, R. M.: Characterization of products formed from the oxidation of toluene and m-xylene with varying NOx and OH exposure, Chemosphere, 334, 139002, https://doi.org/10.1016/j.chemosphere.2023.139002, 2023.

Stark, H., Yatavelli, R. L. N., Thompson, S. L., Kang, H., Krechmer, J. E., Kimmel, J. R., Palm, B. B., Hu, W., Hayes, P. L., Day, D. A., Campuzano-Jost, P., Canagaratna, M. R., Jayne, J. T., Worsnop, D. R., and Jimenez, J. L.: Impact of Thermal Decomposition on Thermal Desorption Instruments: Advantage of Thermogram Analysis for Quantifying Volatility Distributions of Organic Species, Environ. Sci. Technol., 51, 8491–8500, https://doi.org/10.1021/acs.est.7b00160, 2017.

Su, T. and Chesnavich, W. J.: Parametrization of the ion–polar molecule collision rate constant by trajectory calculations, The Journal of Chemical Physics, 76, 5183–5185, https://doi.org/10.1063/1.442828, 1982.

Svendby, T. M., Lazaridis, M., and Tørseth, K.: Temperature dependent secondary organic aerosol formation from terpenes and aromatics, J Atmos Chem, 59, 25–46, https://doi.org/10.1007/s10874-007-9093-7, 2008.

Takekawa, H., Minoura, H., and Yamazaki, S.: Temperature dependence of secondary organic aerosol formation by photo-oxidation of hydrocarbons, Atmospheric Environment, 37, 3413–3424, https://doi.org/10.1016/S1352-2310(03)00359-5, 2003.

Tani, A., Hayward, S., and Hewitt, C. N.: Measurement of monoterpenes and related compounds by proton transfer reaction-mass spectrometry (PTR-MS), International Journal of Mass Spectrometry, 223–224, 561–578, https://doi.org/10.1016/S1387-3806(02)00880-1, 2003.

Thangavel, P., Park, D., and Lee, Y.-C.: Recent Insights into Particulate Matter (PM2.5)-Mediated Toxicity in Humans: An Overview, IJERPH, 19, 7511, https://doi.org/10.3390/ijerph19127511, 2022.

Tian, L., Huang, D. D., Wang, Q., Zhu, S., Wang, Q., Yan, C., Nie, W., Wang, Z., Qiao, L., Liu, Y., Qiao, X., Guo, Y., Zheng, P., Jing, S., Lou, S., Wang, H., Yu, J. Z., Huang, C., and Li, Y. J.: Underestimated Contribution of Heavy Aromatics to Secondary Organic Aerosol Revealed by Comparative Assessments Using New and Traditional Methods, ACS Earth Space Chem., 7, 110–119, https://doi.org/10.1021/acsearthspacechem.2c00252, 2023.

Tomaz, S.: Etude des composés polyaromatiques dans l'atmosphère: caractérisation moléculaire et processus réactionnels en lien avec l'aérosol organique, Université de Lille, 2015.

Virtanen, A., Joutsensaari, J., Koop, T., Kannosto, J., Yli-Pirilä, P., Leskinen, J., Mäkelä, J. M., Holopainen, J. K., Pöschl, U., Kulmala, M., Worsnop, D. R., and Laaksonen, A.: An amorphous solid state of biogenic secondary organic aerosol particles, Nature, 467, 824–827, https://doi.org/10.1038/nature09455, 2010.

Volkamer, R., Jimenez, J. L., San Martini, F., Dzepina, K., Zhang, Q., Salcedo, D., Molina, L. T., Worsnop, D. R., and Molina, M. J.: Secondary organic aerosol formation from anthropogenic air pollution: Rapid and higher than expected, Geophysical Research Letters, 33, 2006GL026899, https://doi.org/10.1029/2006GL026899, 2006.

Wang, L., Atkinson, R., and Arey, J.: Dicarbonyl Products of the OH Radical-Initiated Reactions of Naphthalene and the C_1- and C_2-Alkylnaphthalenes, Environ. Sci. Technol., 41, 2803–2810, https://doi.org/10.1021/es0628102, 2007.

Warren, B., Austin, R. L., and Cocker, D. R.: Temperature dependence of secondary organic aerosol, Atmospheric Environment, 43, 3548–3555, https://doi.org/10.1016/j.atmosenv.2009.04.011, 2009.

Wei, W., Mandin, C., Blanchard, O., Mercier, F., Pelletier, M., Le Bot, B., Glorennec, P., and Ramalho, O.: Temperature dependence of the particle/gas partition coefficient: An application to predict indoor gas-phase concentrations of semi-volatile organic compounds, Science of The Total Environment, 563–564, 506–512, https://doi.org/10.1016/j.scitotenv.2016.04.106, 2016.

Wu, K., Duan, M., Zhou, J., Zhou, Z., Tan, Q., Song, D., Lu, C., and Deng, Y.: Sources Profiles of Anthropogenic Volatile Organic Compounds from Typical Solvent Used in Chengdu, China, J. Environ. Eng., 146, 05020006, https://doi.org/10.1061/(ASCE)EE.1943-7870.0001739, 2020.

Xu, J., Griffin, R. J., Liu, Y., Nakao, S., and Cocker, D. R.: Simulated impact of NO x on SOA formation from oxidation of toluene and m -xylene, Atmospheric Environment, 101, 217–225, https://doi.org/10.1016/j.atmosenv.2014.11.008, 2015.

Xu, L., Kollman, M. S., Song, C., Shilling, J. E., and Ng, N. L.: Effects of NO_x on the Volatility of Secondary Organic Aerosol from Isoprene Photooxidation, Environ. Sci. Technol., 48, 2253–2262, https://doi.org/10.1021/es404842g, 2014.

Xuan, L., Ma, Y., Xing, Y., Meng, Q., Song, J., Chen, T., Wang, H., Wang, P., Zhang, Y., and Gao, P.: Source, temporal variation and health risk of volatile organic compounds (VOCs) from urban traffic in harbin, China, Environmental Pollution, 270, 116074, https://doi.org/10.1016/j.envpol.2020.116074, 2021.

Yamasaki, Hiroyasu., Kuwata, Kazuhiro., and Miyamoto, Hiroko.: Effects of ambient temperature on aspects of airborne polycyclic aromatic hydrocarbons, Environ. Sci. Technol., 16, 189–194, https://doi.org/10.1021/es00098a003, 1982.

Ye, F., Li, J., Gao, Y., Wang, H., An, J., Huang, C., Guo, S., Lu, K., Gong, K., Zhang, H., Qin, M., and Hu, J.: The role of naphthalene and its derivatives in the formation of secondary organic aerosol in the Yangtze River Delta region, China, Atmos. Chem. Phys., 24, 7467–7479, https://doi.org/10.5194/acp-24-7467-2024, 2024.

Zhang, H., Li, H., Zhang, Y., Wang, X., Bi, F., Meng, L., Li, Y., Zhao, L., Zhang, X., Peng, Z., Mu, Y., Mellouki, W., and Chai, F.: Synergistic generation mechanisms of SOA and ozone from the photochemical oxidation of 1,3,5-trimethylbenzene: Influence of precursors ratio, temperature and radiation intensity, Atmospheric Research, 293, 106924, https://doi.org/10.1016/j.atmosres.2023.106924, 2023.

Zhang, J., Choi, M., Ji, Y., Zhang, R., Zhang, R., and Ying, Q.: Assessing the Uncertainties in Ozone and SOA Predictions due to Different Branching Ratios of the Cresol Pathway in the Toluene-OH Oxidation Mechanism, ACS Earth Space Chem., 5, 1958–1970, https://doi.org/10.1021/acsearthspacechem.1c00092, 2021.

Zhang, P., Huang, J., Shu, J., and Yang, B.: Comparison of secondary organic aerosol (SOA) formation during o-, m-, and p-xylene photooxidation, Environmental Pollution, 245, 20–28, https://doi.org/10.1016/j.envpol.2018.10.118, 2019a.

Zhang, Q., Xu, Y., and Jia, L.: Secondary organic aerosol formation from OH-initiated oxidation of <i>m</i>-xylene: effects of relative humidity on yield and chemical composition, Atmos. Chem. Phys., 19, 15007–15021, https://doi.org/10.5194/acp-19-15007-2019, 2019b.

Zhao, D., Schmitt, S. H., Wang, M., Acir, I.-H., Tillmann, R., Tan, Z., Novelli, A., Fuchs, H., Pullinen, I., Wegener, R., Rohrer, F., Wildt, J., Kiendler-Scharr, A., Wahner, A., and Mentel, T. F.: Effects of NO_x and SO_2 on the secondary organic aerosol formation from photooxidation of α -pinene and limonene, Atmos. Chem. Phys., 18, 1611–1628, https://doi.org/10.5194/acp-18-1611-2018, 2018.

Zhao, J., Zhang, R., Misawa, K., and Shibuya, K.: Experimental product study of the OH-initiated oxidation of m-xylene, Journal of Photochemistry and Photobiology A: Chemistry, 176, 199–207, https://doi.org/10.1016/j.jphotochem.2005.07.013, 2005.

Zhou, X.: The gas/particle partitioning behavior of phthalate esters in indoor environment: Effects of temperature and humidity, Environmental Research, 2021.

Zhu, M., Huang, M., Xue, B., Cai, S., Hu, C., Zhao, W., Gu, X., and Zhang, W.: Chemical analysis of nitro-aromatic compounds of secondary organic aerosol formed from photooxidation of p-xylene with NO *x*, J Chinese Chemical Soc, 68, 1697–1708, https://doi.org/10.1002/jccs.202100105, 2021.

Supporting Information for:

Gas-particle partitioning of m-xylene and naphthalene oxidation products: temperature and NO_x influence

Marwa Shahin[1], Julien Kammer[1], Brice Temime-Roussel[1], and Barbara D'Anna[1]

[1]Aix-Marseille Univ., CNRS, LCE, Marseille, France

Supplementary method

Calculation of the carbon balance

The carbon balance was calculated by comparing the total carbon content of detected reaction products to the amount of carbon from the reacted precursor VOCs, with all quantities expressed in units of ppbC. First, the amount of precursor carbon reacted was determined by:

$$reacted\ carbon\ (ppbC)\ =\ \Delta[VOC]\ (ppb)\ \times\ n_C$$

where $\Delta[VOC]$ is the decrease in the VOC concentration due to its reaction, and n_C is the number of carbon atoms per molecule (8 for m-xylene, 10 for naphthalene).

Second, the carbon content of all observed products was calculated by summing the contribution of each compound:

$$product\ carbon\ (ppbC)\ =\ \sum_i ([product_i]\ (ppb)\ \times\ n_{C,i})$$

where $[product_i]$ is the measured mixing ratio and $n_{C,i}$ is the carbon number of each compound i.

The carbon balance was then computed as:

$$carbon\ balance\ (\%)\ =\ \frac{product\ carbon\ (ppbC)}{reacted\ carbon\ (ppbC)}\ \times\ 100$$

This calculation assumes that all carbon is either retained in the measured gas-phase or particle-phase products or converted into undetected species. It does not account for potential carbon in undetected products (e.g., oligomers, extremely low volatility species), or known small carbon products such as CO, CO_2, and glyoxal that we could not measure because of instrumental limitations.

Calculation of the OH rate constant

The values of the temperature dependent OH rate constant are calculated based on Arrhenius equation as follows:

$$k_{OH}\ (T)\ =\ A\ \frac{T}{298\ (K)}\ e^{\frac{-Ea}{RT}}$$

where

- k_{OH} (T) is the rate constant at temperature (T) [cm^3 $molecule^{-1}$ s^{-1}]
- T is the temperature [K]
- A is the pre-exponential factor
- R is the universal gas constant [8.413 J mol^{-1} K^{-1}]
- Ea is the activation energy [J mol^{-1}]

The specific parameters were (taken from NIST Kinetic Database):

- m-xylene: A = 1.66×10^{-11}, Ea = -964 J mol^{-1}
- naphthalene: A = 1.05×10^{-12}, Ea = -7500 J mol^{-1}

Calculation of the TSP

The SMPS measures number- and volume-based size distributions. In our analysis, we used the number concentration (particles cm^{-3}) measured by the SMPS and converted it to mass concentration (μg m^{-3}) by assuming spherical particles and applying the standard geometric volume formula for each size bin. Each calculated particle volume was then multiplied by the assumed composition-specific density to determine mass. Specifically, the densities used were: 1.0 g cm^{-3} for water, 1.4 g cm^{-3} for organics, and 1.7 g cm^{-3} for ammonium, sulfate and nitrate. The percentage of each chemical fraction for each experiment was inferred from AMS measurements, and the corresponding weighted average density was applied to the SMPS volume distribution to obtain TSP. This approach provided a more accurate representation of the aerosol mass.

Table S1. List of laboratory experiments conducted by Ng et al. (2007), Chen et al. (2018), Song et al. (2007), Chen et al. (2016) Chen et al. (2009), and their associated environmental conditions, such as chamber temperature, RH, VOC/NO_x ratio, seeds mass and SOA yields.

	T	**RH**	**VOC**	**NO_x**	**VOC/NO_x**	**Seeds**	**[OH]**	**ΔVOC**	**ΔM_0**	***Y***
	K	%	ppbV	ppb	ppbC ppb^{-1}	$\mu g\ m^{-3}$	molecules cm^{-3}	$\mu g\ m^{-3}$	$\mu g\ m^{-3}$	%
Ng et al. (2007)	297	6	42-172 (not indicated for each exp)	943	high NO_x	AS	from HONO	71	18	5.9
	298	6		945	high NO_x	AS		28	4	3.5
	298	6		943	high NO_x	AS		133	46	8
	297	5		945	high NO_x	AS		106	37	8
Chen et al. (2018)	300	<0.1	44	8	high NO_x	none	3.04E+06	159	4.8	3
	300	<0.1	59	11.5	high NO_x	none	2.79E+06	201	11.6	6
Song et al. (2007)	300	<0.1	104	-	low NO_x	none	0.55E+06	193	17.3	8.9
	300	<0.1	112	-	low NO_x	none	0.84E+06	227	38	16.7
	300	<0.1	51	-	low NO_x	none	0.80E+06	113	20	17.7
	300	<0.1	39	-	low NO_x	none	1.05E+06	97	11.9	12.3
	300	<0.1	52	-	low NO_x	none	1.29E+06	147	45	30.6
	300	<0.1	46	-	low NO_x	none	1.18E+06	124	25	20.6
Chen et al. (2016)	RT	<0.1	45	698	high NO_x	none	from HONO	168	94.8	60
	RT	<0.1	29	776	high NO_x	none		126	59.4	47
	RT	<0.1	26	758	high NO_x	none		116	47.1	41
	RT	<0.1	30	776	high NO_x	none		105	3	3
	RT	<0.1	23	783	high NO_x	none		80	20.3	25
	RT	<0.1	28	22	low NO_x	none		135	5.7	4
	RT	<0.1	15	13	low NO_x	none		76	21.1	28
	RT	<0.1	27	19	low NO_x	none		140	30.8	22
	RT	<0.1	35	10	low NO_x	none		173	50.1	29
	RT	<0.1	29	18	low NO_x	none		142	27.1	19
	RT	<0.1	17	11	low NO_x	none		84	26.2	31
	RT	<0.1	17	14	low NO_x	17.3		86	15.5	18
	RT	<0.1	16	21	low NO_x	41.9		77	9.7	13
	RT	<0.1	27	18	low NO_x	15.4		125	34.5	28
	RT	<0.1	15	10	low NO_x	3.4		69	22.7	33

Chan et al. (2009)	299	5-8	12	494	high NO_x	AS		59	10.9	19
	299	5-8	21	377	high NO_x	AS		93	27.7	30
	299	5-8	10	424	high NO_x	AS	from HONO	40	8	20
	299	5-8	17	477	high NO_x	AS		65	13.6	21
	299	5-8	17	477	high NO_x	AS		84	22.8	27

49

Table S2. Derived and estimated $\log_{10}C_i^*$ values for m-xylene products

Carbon number	Measured m/z and ion sum formula	Tentative assignment	SMILES string	Derived values			Estimated values		
				$\log_{10}C_i^*$ at 295 K	$\log_{10}C_i^*$ at 280 K	$\Delta\log_{10}C_i^*$	$\log_{10}C_i^*$ at 295 K	$\log_{10}C_i^*$ at 280 K	$\Delta\log_{10}C_i^*$
8	121.06 (C_8H_8O).H^+	tolualdehdye	CC1=CC(=CC=C1)C=O	3.72	3.66	0.06	6.03	5.65	0.38
8	171.07 ($C_8H_{10}O_4$).H^+	dimethyl-hexadienedioic acid	C/C(=C\C(=O)O)/C=C(\C)/C(=O)O	1.12	0.83	0.30	0.87	0.30	0.58
		dihydroxy-dimethyl-cyclohexene-dine	CC1=CC(=O)C(C(C1=O)(C)O)O				0.78	0.21	0.58
8	153.06 ($C_8H_8O_3$).H^+	hydroxy-methylbenzoic acid	Cc1cccc(C(=O)O)c1O	2.19	2.07	0.12	1.78	1.29	0.49
8	187.06 ($C_8H_{10}O_5$).H^+	oxo-cyclohexane-dicarboxylic acid	C1C(CC(=O)CC1C(=O)O)C(=O)O	0.78	0.69	0.09	0.19	-0.45	0.64
		hydroxy-cyclohexene-dicarboxylic acid	C(C(=O)O)1C(C(O)=O)CC=CC1O				-1.19	-1.95	0.76
7	141.05 ($C_7H_8O_3$).H^+	oxohepta-dienoic acid	CC(=O)/C=C/C=C/C(=O)O	1.74	1.41	0.33	3.86	3.33	0.53
7	154.05 ($C_7H_7NO_3$).H^+	nitrocresol	Cc1c(cccc1O)[N+](=O)[O-]	2.51	2.39	0.12	5.83	5.37	0.46
6	127.04 ($C_6H_6O_3$).H^+	dimethyl furandione	CC1=C(C)C(=O)OC1=O	1.95	1.79	0.17	5.46	5.06	0.40
6	129.06 ($C_6H_8O_3$).H^+	hydroxy-dioxohexanal	CC(=O)C(O)CC(=O)C=O	1.73	1.31	0.43	3.58	3.07	0.52
		methyl-oxo-pentenoic acid	CC(=CC(=O)O)C(=O)C				4.36	3.87	0.49
5	113.02 ($C_5H_4O_3$).H^+	methylfuran-dione	CC1=CC(=O)OC1=O	3.45	3.11	0.34	5.85	5.46	0.39
5	131.04 ($C_5H_6O_4$).H^+	hydroxy-methyl-oxosuccinaldehyde	CC(C=O)(C(=O)C=O)O	2.54	2.13	0.40	3.55	3.11	0.43
5	115.03 ($C_5H_6O_3$).H^+	oxopentenoic acid	C=CC(=O)CC(=O)O	2.14	1.72	0.41	4.74	4.27	0.47
5	97.03 ($C_5H_4O_2$).H^+	furaldehyde (furfural)	C1=COC(=C1)C=O	2.56	2.27	0.30	6.52	6.18	0.34
5	117.05 ($C_5H_8O_3$).H^+	oxo-pentanoic acid	CC(=O)CCC(=O)O	2.62	2.00	0.62	4.85	4.39	0.46
5	101.06 ($C_5H_8O_2$).H^+	oxo-pentanal	CC(=O)CCC=O	1.99	1.40	0.59	6.99	6.64	0.35
4	71.05 (C_4H_6O).H^+	dihydrofuran	C1COC=C1	2.90	2.26	0.65	8.75	8.51	0.24
		MVK	CC(=O)C=C				8.51	8.24	0.27
		MAC	CC(=C)C=O				8.10	7.83	0.26
4	103.04 ($C_4H_6O_3$).H^+	hydroxy oxobutanal	C(CO)C(=O)C=O	1.76	0.84	0.92	5.23	4.79	0.44
3	73.03 ($C_3H_4O_2$).H^+	methylglyoxal	CC(=O)C=O	3.16	2.69	0.47	7.72	7.45	0.27

3	75.04 ($C_3H_6O_2$).H^+	propanoic acid	CCC(=O)O	3.26	3.06	0.20	6.45	6.10	0.35

Table S3. Derived and estimated $\log_{10}C_i^*$ values for naphthalene products

Carbon number	Measured m/z and ion sum formula	Tentative assignment	SMILES string	Derived values			Estimated values		
				$\log_{10}C_i^*$ at 295 K	$\log_{10}C_i^*$ at 280 K	$\Delta\log_{10}C_i^*$	$\log_{10}C_i^*$ at 295 K	$\log_{10}C_i^*$ at 280 K	$\Delta\log_{10}C_i^*$
10	161.06 ($C_{10}H_8O_2$).H^+	formyl cinnamaldehyde	C1=CC=C(C(=C1)/C=C/C=O)C=O	1.91	1.20	0.71	3.85	3.25	0.60
10	193.05 ($C_{10}H_8O_4$).H^+	carboxy cinnamic acid	O=C(O)/C=C/c1ccccc1C(=O)O	1.28	1.15	0.13	-0.52	-1.17	0.65
10	159.04 ($C_{10}H_6O_2$).H^+	naphthoquinone	c1ccc2c(c1)C(=O)C=CC2=O	2.61	1.79	0.82	4.65	4.16	0.49
10	177.05 ($C_{10}H_8O_3$).H^+	formyl cinnamic acid	O=Cc1ccccc1/C=C/C(=O)O	1.44	1.24	0.20	1.66	1.07	0.60
10	175.04 ($C_{10}H_6O_3$).H^+	epoxy-naphthoquinone	C1=CC=CC2C(=O)C3OC3C(=O)C1=2	1.82	1.68	0.14	4.12	3.54	0.58
10	145.07 ($C_{10}H_8O$).H^+	naphthol	c1ccc2c(c1)cccc2O	1.75	1.21	0.54	3.78	3.28	0.50
10	191.04 ($C_{10}H_6O_4$).H^+	dihydroxy naphthoquinone	C1=C(O)C(O)=CC2C(=O)C=CC(=O)C1=2	1.81	1.66	0.15	0.49	-0.25	0.74
10	195.06 ($C_{10}H_{10}O_4$).H^+	phenylenediacetic acid	c1ccc(c(c1)CC(=O)O)CC(=O)O	1.79	1.50	0.29	-0.41	-1.05	0.64
		carboxybenzenepropanoic acid	c1ccc(c(c1)CCC(=O)O)C(=O)O				-0.42	-1.04	0.63
10	174.05 ($C_{10}H_7NO_2$).H^+	nitronaphthalene	c1ccc2c(c1)cccc2[N+](=O)[O-]	3.07	2.32	0.75	3.85	3.37	0.48
10	190.05 ($C_{10}H_7NO_3$).H^+	nitronaphthol	c1ccc2c(c1)c(ccc2O)[N+](=O)[O-]	1.81	1.58	0.23	3.94	3.38	0.55
9	147.05 ($C_9H_6O_2$).H^+	benzopyrone (coumarin)	c1ccc2c(c1)ccc(=O)o2	2.16	1.60	0.56	5.16	4.67	0.49
		indene-dione	c1ccc2c(c1)C(=O)CC2=O				5.16	4.66	0.50
9	163.04 ($C_9H_6O_3$).H^+	hydroxycoumarin	c1ccc2c(c1)c(cc(=O)o2)O	1.90	1.75	0.15	3.08	2.50	0.58
9	133.06 (C_9H_8O).H^+	indanone	c1ccc2c(c1)CCC2=O	2.63	1.63	1.00	5.37	4.94	0.44
9	179.04 ($C_9H_6O_4$).H^+	dihydroxy-indene-dione	C1=CC=CC2C(=O)C(O)(O)C(=O)C1=2	1.63	0.54	1.08	3.05	2.35	0.69
9	165.06 ($C_9H_8O_3$).H^+	hydroxy cinnamic acid	c1ccc(c(c1)/C=C/C(=O)O)O	2.05	1.61	0.44	1.28	0.70	0.58
9	181.05 ($C_9H_8O_4$).H^+	dihydroxycinnamic acid	C1=CC(O)=CC(/C=C/C(=O)O)=C1O	1.64	1.41	0.23	-0.80	-1.51	0.70

8	135.05 ($C_8H_6O_2$).H^+	phthaldialdehyde	O=Cc1ccccc1C=O	3.32	2.16	1.06	4.73	4.27	0.46
8	149.03 ($C_8H_4O_3$).H^+	phthalic anhydride	c1ccc2c(c1)C(=O)OC2=O	3.16	2.76	0.39	5.10	4.62	0.49
8	151.04 ($C_8H_6O_3$).H^+	hydroxy phthalide	C1=CC=CC(C(=O)O)=C1C=O	2.11	1.50	0.61	2.57	2.02	0.55
		hydroxy phthalaldehyde	C1=CC(O)=CC(C=O)=C1C=O				2.65	2.11	0.54
6	115.07 ($C_6H_{10}O_2$).H^+	dimethyloxolanone	CC1CC(OC1=O)C	3.24	2.40	0.84	7.73	7.33	0.40
		hexanedione	CC(=O)CCC(=O)C				7.03	6.65	0.38

52

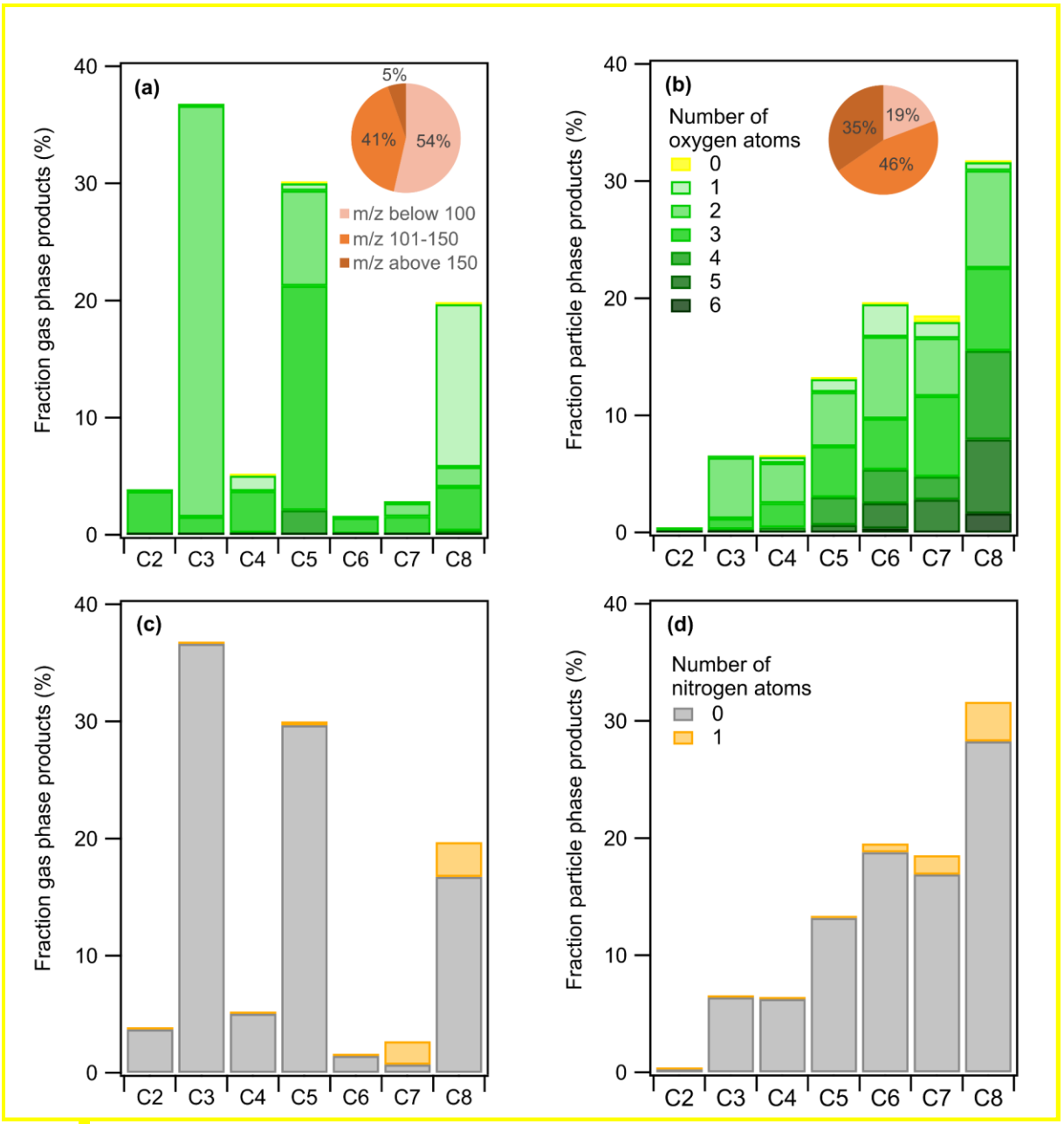

Figure S1. m-xylene mass products fraction (y-axis) distribution based on the number of carbon atoms (x-axis) for a high NO_x experiment 295 K, colored by the number of (a,b) oxygen and (c,d) nitrogen atoms. Detected compounds are in the (a,c) gas phase and (b,d) particle phase. Pie charts correspond to the molecular weight contribution to the overall mass.

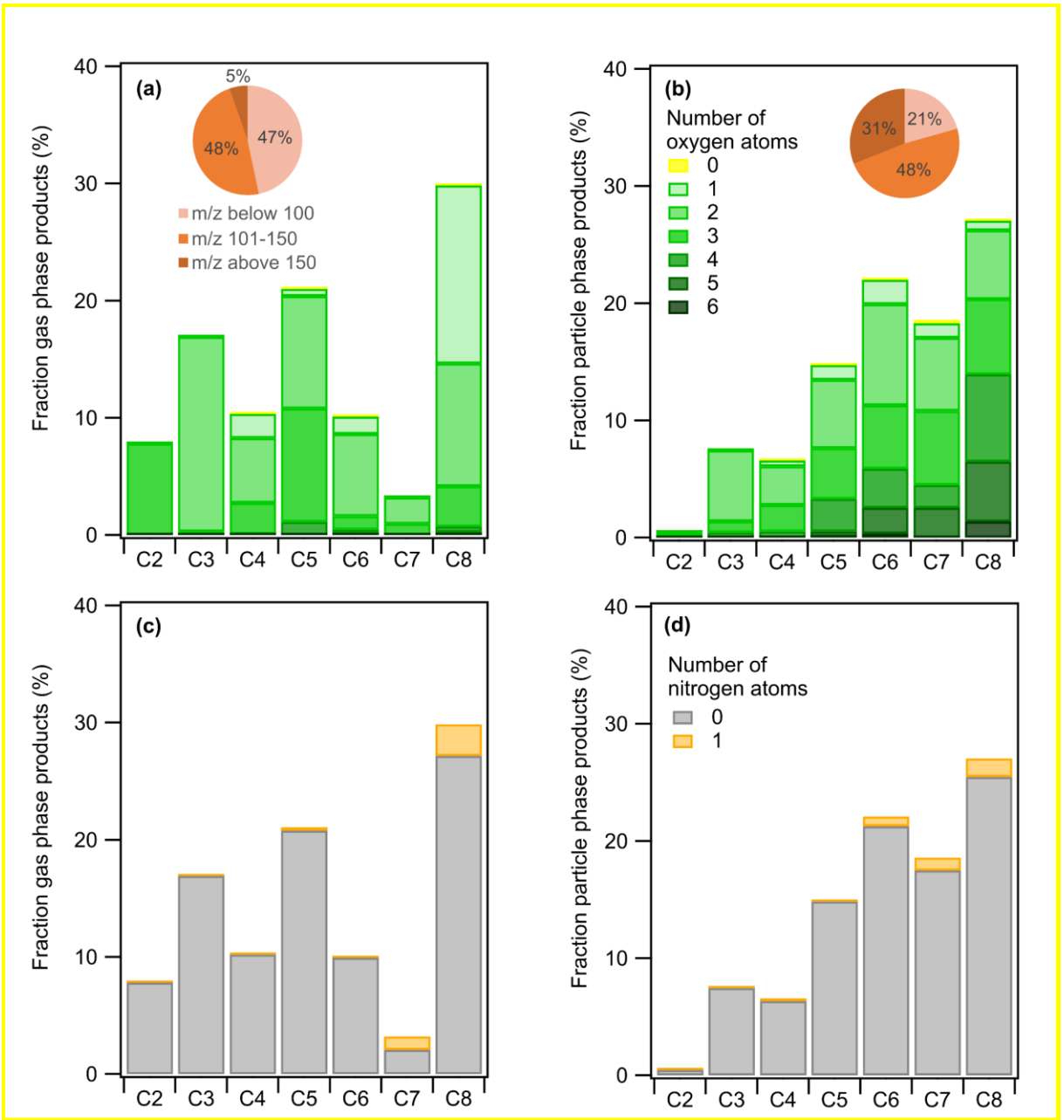

Figure S2. m-xylene mass products fraction (y-axis) distribution based on the number of carbon atoms (x-axis) for a low NO_x experiment 295 K, colored by the number of (a,b) oxygen and (c,d) nitrogen atoms. Detected compounds are in the (a,c) gas phase and (b,d) particle phase. Pie charts correspond to the molecular weight contribution to the overall mass.

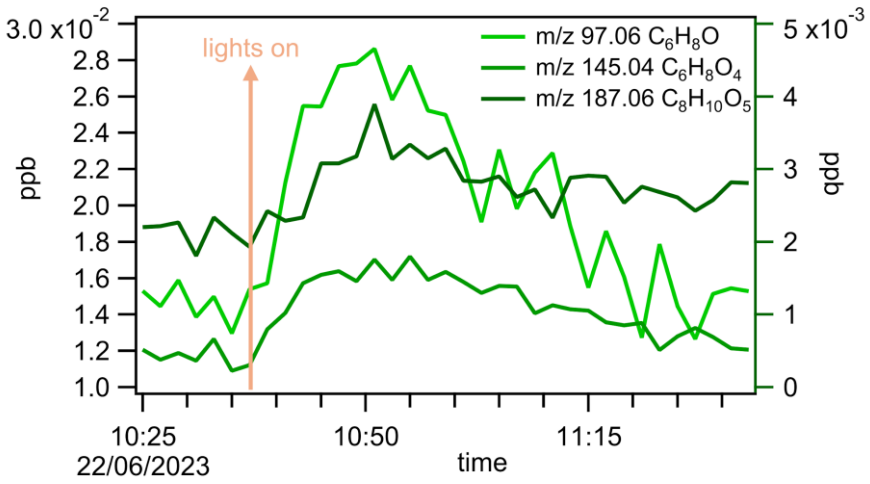

Figure S3. Time evolution of some C_6 and C_8 compounds in the gas phase at 295 K high NO_x experiment upon starting oxidation in the flow tube.

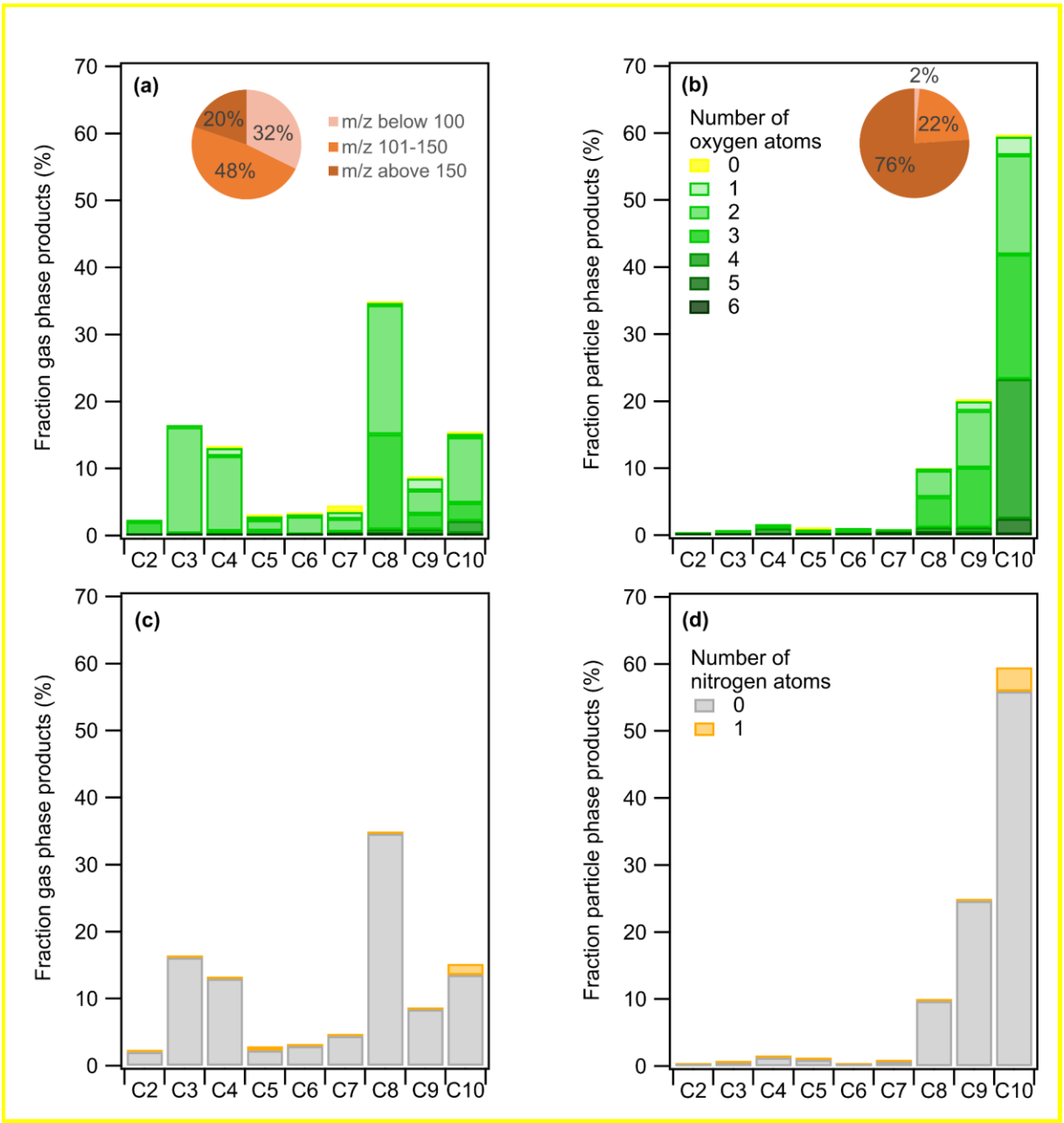

Figure S4. Naphthalene mass products fraction (y-axis) distribution based on the number of carbon atoms (x-axis) for a high NO_x experiment 295 K, colored by the number of (a,b) oxygen and (c,d) nitrogen atoms. Detected compounds are in the (a,c) gas phase and (b,d) particle phase. Pie charts correspond to the molecular weight contribution to the overall mass.

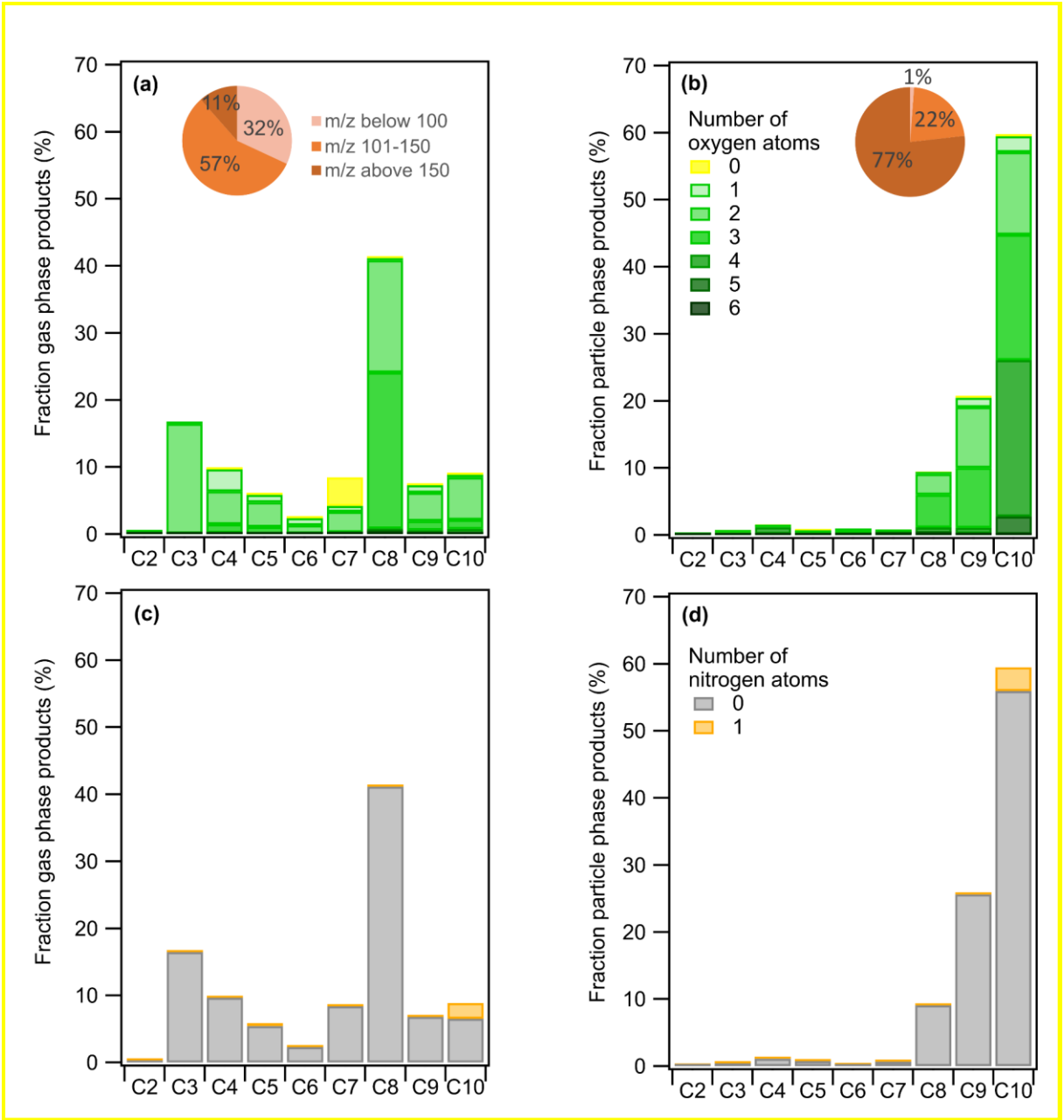

Figure S5. Naphthalene mass products fraction (y-axis) distribution based on the number of carbon atoms (x-axis) for a low NO_x experiment 295 K, colored by the number of (a,b) oxygen and (c,d) nitrogen atoms. Detected compounds are in the (a,c) gas phase and (b,d) particle phase. Pie charts correspond to the molecular weight contribution to the overall mass.

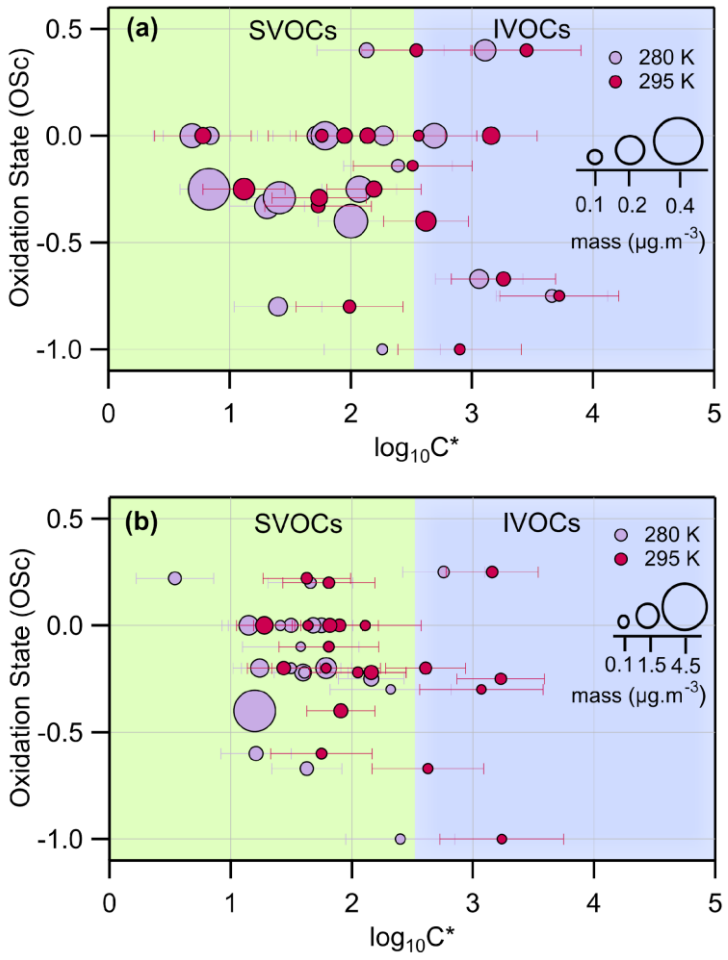

Figure S6. The OSc (y-axis) for the detected parent ions of (a) m-xylene and (b) naphthalene photooxidation, respectively, as a function of saturation concentration ($\log_{10}C_i^*$ in µg m^{-3}; x-axis) for high NO_x experiments. The size of the circles denotes the mass of each species. Experiments carried out at 280 K are in light violet while the ones carried out at 295 K are in magenta.

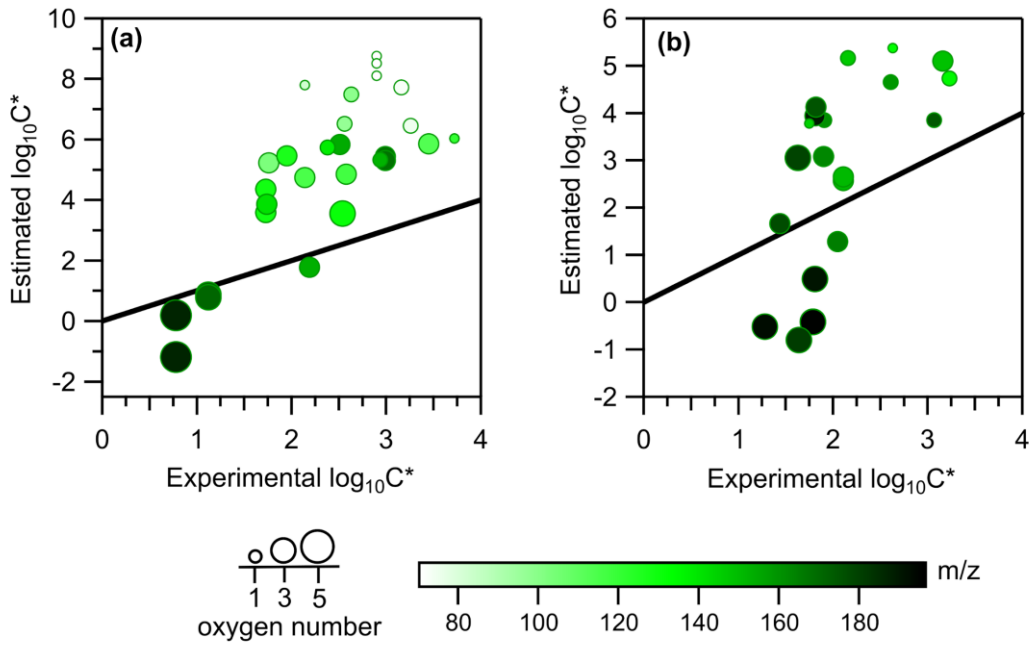

Figure S7. Theoretical (y-axis) versus experimental $\log_{10}C_i^*$ values (x-axis) for (a) m-xylene and (b) naphthalene oxidation products at 295 K under high NO_x conditions. The black line is the 1:1 fit. The size of the markers is proportional to the oxygen number. The color gradient corresponds to *m*/*z* of the detected compounds.

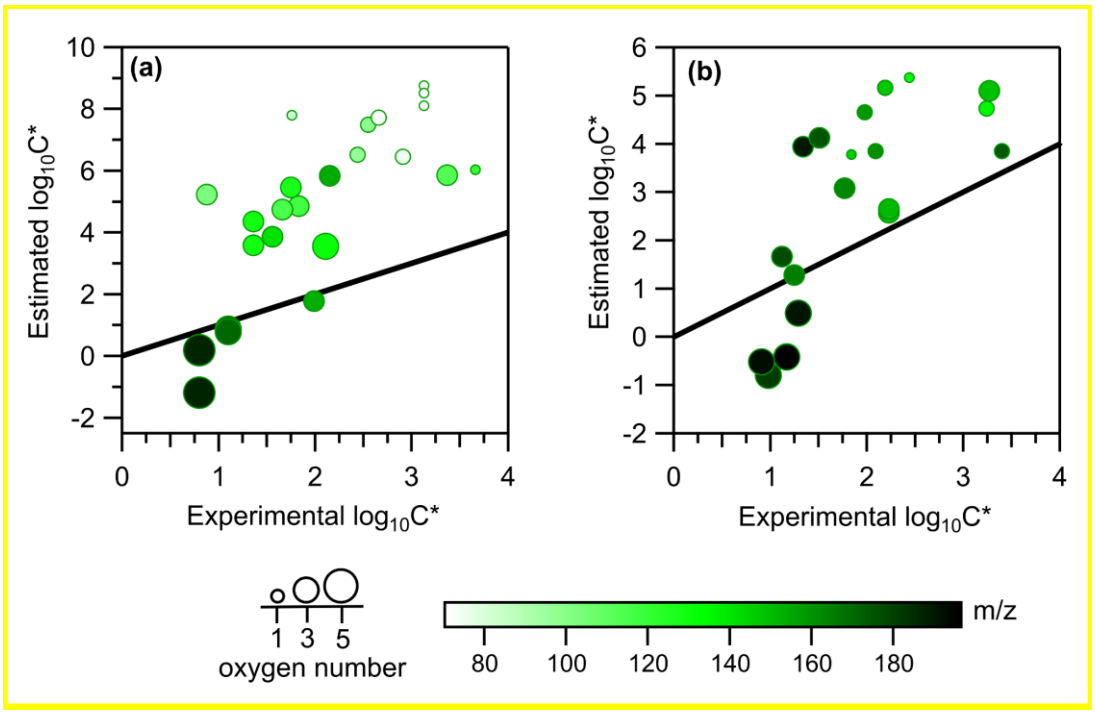

Figure S8. Theoretical (y-axis) versus experimental $\log_{10}C_i^*$ values (x-axis) for (a) m-xylene and (b) naphthalene oxidation products at 295 K under low NO_x conditions. The black line is the 1:1 fit. The size of the markers is proportional to the oxygen number. The color gradient corresponds to *m*/*z* of the detected compounds.

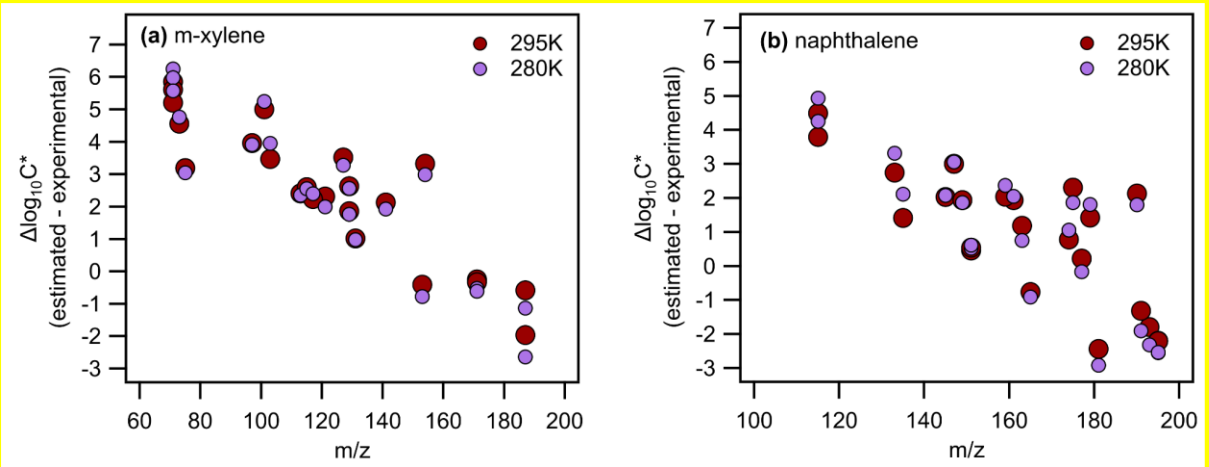

Figure S9. $\Delta\log_{10}C_i^*$ ($\log_{10}C_i^*$ Estimated minus $\log_{10}C_i^*$ Experimental; y-axis) versus m/z (x-axis) for (a) m-xylene and (b) naphthalene oxidation products under high NO_x conditions, at 295 K (magenta) and 280 K (light violet).